



Development of a multiscale model of the human lumbar spine for investigation of tissue loads in people with and without a transtibial amputation during sit-to-stand

Jasmin D. Honegger¹ · Jason A. Actis¹ · Deanna H. Gates² · Anne K. Silverman¹ · Ashlyn H. Munson³ · Anthony J. Petrella¹

Received: 29 January 2020 / Accepted: 19 September 2020 / Published online: 7 October 2020
© Springer-Verlag GmbH Germany, part of Springer Nature 2020

Abstract

Quantification of lumbar spine load transfer is important for understanding low back pain, especially among persons with a lower limb amputation. Computational modeling provides a helpful solution for obtaining estimates of in vivo loads. A multiscale model was constructed by combining musculoskeletal and finite element (FE) models of the lumbar spine to determine tissue loading during daily activities. Three-dimensional kinematic and ground reaction force data were collected from participants with ($n = 4$) and without ($n = 4$) a unilateral transtibial amputation (TTA) during 5 sit-to-stand trials. We estimated tissue-level load transfer from the multiscale model by controlling the FE model with intervertebral kinematics and muscle forces predicted by the musculoskeletal model. Annulus fibrosis stress, intradiscal pressure (IDP), and facet contact forces were calculated using the FE model. Differences in whole-body kinematics, muscle forces, and tissue-level loads were found between participant groups. Notably, participants with TTA had greater axial rotation toward their intact limb ($p = 0.029$), greater abdominal muscle activity ($p < 0.001$), and greater overall tissue loading throughout sit-to-stand ($p < 0.001$) compared to able-bodied participants. Both normalized (to upright standing) and absolute estimates of L4–L5 IDP were close to in vivo values reported in the literature. The multiscale model can be used to estimate the distribution of loads within different lumbar spine tissue structures and can be adapted for use with different activities, populations, and spinal geometries.

Keywords Computational biomechanics · Multiscale model · Finite element analysis · Lumbar spine

1 Introduction

Low back pain (LBP) is common in the general population and is the leading cause of disability worldwide (Vos et al. 2016). In certain subpopulations who experience more extreme repetitive spine kinematics (e.g., gymnasts, cyclists, and people with a lower-limb amputation), the prevalence of LBP is often attributed to biomechanical factors (Svärd

et al. 1991; Wilber et al. 1995; Morgenroth et al. 2010). Repetitive loading of the spine during lumbar movements produces lesions, fractures, injury, and abnormal stresses in innervated elements known to be sources of pain, with examples including: vertebral body fractures, intervertebral disc tears, endplate lesions, and abnormal disc stress (Bogduk 2012). Thus, determining how spine kinematics influence load-transfer within the tissues (i.e., intervertebral discs and facets) during daily activities is important for determining the etiology of population-specific biomechanical LBP.

People with a lower-limb amputation have a greater prevalence of LBP (up to 71%) compared to the general population (Burke et al. 1978; Smith et al. 1999). Altered low back biomechanics have been implicated as one of the primary contributing factors to LBP in people with lower-limb amputations (Devan et al. 2014; Hendershot and Wolf 2014). During walking, people with a transtibial amputation (TTA) have greater trunk-pelvis ranges of motion and greater lateral

✉ Anthony J. Petrella
apetrell@mines.edu

¹ Department of Mechanical Engineering, Colorado School of Mines, Golden, CO 80401, USA

² School of Kinesiology, University of Michigan, Ann Arbor, MI 48109, USA

³ Department of Applied Mathematics and Statistics, Colorado School of Mines, Golden, CO 80401, USA

bending toward the prosthetic limb (Rueda et al. 2013; Hendershot and Wolf 2014; Yoder et al. 2015) linked with greater L4–L5 spinal loads (Yoder et al. 2015). In addition to walking, the sit-to-stand movement is an important activity of daily living that people with TTA perform approximately 50 times a day (Bussmann et al. 2004, 2008). Greater peak and average net compressive lumbar spinal loads have been observed at the L4–L5 level in people with TTA while performing sit-to-stand (Actis et al. 2018b). However, the distribution of these spinal loads within the lumbar spine soft tissue structures is unknown and this information could provide useful insight into potential LBP development in people with TTA.

Lumbar spinal loads have previously been measured *in vivo* by several methods (Dreischarf et al. 2016). Intradiscal pressure (IDP) was measured *in vivo* by the insertion of pressure transducers into the L4–L5 intervertebral disc of volunteers performing a variety of movement tasks (Nachemson and Morris 1964; Nachemson 1965; Nachemson and Elfström 1970; Sato et al. 1999; Wilke et al. 1999, 2001; Takahashi et al. 2006). Forces and moments transmitted through the spine have also been measured *in vivo* with instrumented implants (Rohlmann et al. 1999, 2013) and trunk muscle forces have been measured through the use of surface and deep electromyography (EMG) (Cholewicki et al. 1995; Stokes et al. 2003; Van Dieen and Kingma 2005). *In vitro* disc pressure response has also been measured in porcine and goat intervertebral discs under compressive loading (Emanuel et al. 2018; Nikkhoo et al. 2018). While these methods supply insightful information about measurements of spinal loading, they have limitations. *In vivo* methods are invasive and typically do not provide simultaneous information of spinal loading at multiple lumbar levels and within different soft tissue structures. *In vitro* methods do not account for the role of active structures, are not measured in living humans, and are not measured during different daily activities.

Computational modeling techniques provide a solution for estimation of biomechanical quantities that are difficult or impossible to measure *in vivo*. Musculoskeletal models of the lumbar spine and thorax have been previously developed and used to estimate spinal muscle force distribution and joint contact loads [i.e., De Zee et al. (2007), Christophy et al. (2012), Han et al. (2012), Bruno et al. (2015), Ignasiak et al. (2016), Bassani et al. (2017), Bayoglu et al. (2017), Actis et al. (2018a), Beaucage-Gauvreau et al. (2019)]. Although these models provide useful information about spinal biomechanics, musculoskeletal models only estimate net joint contact forces and lack the capability to estimate the distribution of loads within the soft tissues. Finite element (FE) models of the lumbar spine have been used to estimate lumbar spine tissue loads (i.e., facet contact forces, intervertebral disc pressures, and annulus stresses) across a

variety of participants and using different modeling methods (i.e., Schmidt et al. (2010), Lalonde et al. (2013), Dreischarf et al. (2014), Campbell et al. (2016), Xu et al. (2017), Lavecchia et al. (2018), Rohlmann et al. (2006), Ghezlbash et al. (2019a), Liu et al. (2018)]. However, FE models are often driven by simplified boundary conditions, lacking physiological motion and loads estimated *in vivo*.

There are a few studies that have used detailed medical image-based *in vivo* kinematics to drive FE models of the spine [i.e., Zanjani-Pour et al. (2018, (2016), Dehghan-Hamani et al. (2019), Affolter et al. (2020)]. This modeling strategy allows for tissue loads to be predicted by participant-specific vertebral displacements. However, image-based methods put participants at risk for increased radiation exposure (Brenner and Hall 2007; Verdun et al. 2008), which can be difficult to justify clinically. In addition, FE models alone still lack anatomical detail and biomechanical information (i.e., whole-body kinematics and kinetics) for other portions of the body that may be useful for understanding relationships between whole-body movements and tissue-level loading.

Some groups have combined musculoskeletal and FE modeling methods for the spine [e.g., Zhu et al. (2013), Tomanidou and Noailly (2015), Shojaei et al. (2016), Azari et al. (2018), Khoddam-Khorasani et al. (2018), Liu et al. (2018)]. This multiscale approach enables estimation of tissue loads driven by physiological kinematics and loading within a single simulation framework. These previously developed models provide additional insight into spinal biomechanics that are lacking when musculoskeletal and FE models are used separately. However, many published models are either limited by prescribed static positions or lack of certain soft tissue details such as ligament, facet, or disc material characterization.

For populations that develop LBP as a result of altered low back biomechanics, such as people with a lower-limb amputation (Devan et al. 2014; Hendershot and Wolf 2014), the development of a modeling framework that uses *in vivo* kinematics to investigate low back tissue loads in structures known to be susceptible to fatigue failure and LBP (e.g., facets, vertebral bodies, and intervertebral discs) (Bogduk 2012) could be beneficial. This information can provide detailed insight into injury risk and pain development to aid in targeted rehabilitation, which is still substantially lacking for people with both LBP and a lower-limb amputation (Highsmith et al. 2019). A first step toward this goal was taken by a previous study that employed a modeling framework to investigate trunk muscle forces and spinal loads in people with a unilateral, transfemoral amputation during sit-to-stand and stand-to-sit (Shojaei et al. 2019). Using a nonlinear FE model, the study found that people with a transfemoral amputation had larger peak and mean spinal loads compared to able-bodied controls and further suggested

that greater spinal loads across the range of daily activities may cause fatigue failure of the spine. While this study is a valuable first step, the spinal loads investigated were net compressive and shear spinal loads and it is unknown how those loads are distributed within the different soft tissues of the spine. No previous study has investigated lumbar spine soft tissue loads during a dynamic activity for people in two distinct population groups (i.e., people with and without a lower-limb amputation).

Therefore, the purpose of this study was to develop a detailed multiscale model of the lumbar spine driven by experimental *in vivo* biomechanics to answer the following questions: (1) What loads develop within the tissue structures of the lumbar spine for individuals with and without TTA during sit-to-stand (which is an important activity of daily living)? (2) Is there a relationship between an individual's lumbar spine kinematics and the resulting tissue loads? The sit-to-stand movement was simulated based on measured whole-body kinematics and kinetics. Participant-specific lumbar spine muscle force distribution, joint contact loads, intervertebral motion, and tissue-level loads were estimated. We compared trunk-pelvis kinematics, trunk muscle forces, joint loads, and tissue-level loads between groups. Estimates of L4–L5 intradiscal pressure for all participants were compared to *in vivo* values measured during sit-to-stand from Wilke et al. (2001) for indirect validation. We expected to observe greater trunk-pelvis ranges of motion, trunk muscle forces, net joint loads, and tissue-level loads in participants with TTA compared to able-bodied participants. We also expected to observe good agreement between model estimates of L4–L5 intradiscal pressure and *in vivo* measurements.

2 Methods

2.1 Musculoskeletal model

Whole-body musculoskeletal models with lumbar spine fidelity were developed in OpenSim v3.3 (simtk.org) for people with and without TTA. Briefly, the able-bodied model contained 294 Hill-type musculotendon actuators, 18 body segments (torso, five lumbar vertebrae, sacrum, pelvis as well as the left and right thigh, shank, calcaneus, talus, and toes), and 19 degrees of freedom (DOF) with the motion of the five lumbar intervertebral joints constrained by a kinematic rhythm that represented each rotational DOF as a linear function of the total trunk-pelvis motion (Christophy et al. 2012). The version of the model with TTA was created by removing 12 ankle muscles of the residual limb, reducing the residual shank mass, and shifting residual shank center-of-mass proximally following methods described by Silverman and Neptune (2012). The prosthetic ankle was modeled using an idealized

torque actuator similar to Actis et al. (2018b). Both models (with and without TTA) have been validated against *in vivo* measurements of muscle activations and L4–L5 joint loading during trunk-pelvis range of motion tasks (Actis et al. 2018a), and muscle activations have shown good agreement with EMG measurements during sit-to-stand Actis et al. (2018b). In addition, the musculoskeletal models were enhanced by implementing 3-DOF bushing elements at each intervertebral joint level to represent the net passive stiffness of the surrounding soft tissues (intervertebral discs, spinal ligaments, and facet joint capsules) (Senteler et al. 2016).

2.2 Finite element model

An FE model of the ligamentous lumbar spine created in Abaqus/Standard (Simulia, Johnston, RI, USA) replaced the L1–L5 geometry of the musculoskeletal model. The FE model has been previously validated for moment-rotation response (*in vivo* data), disc pressure (*in vivo*), and facet force (*in vitro*) during the six primary bending modes of the lumbar spine (flexion, extension, left/right axial rotation, and left/right lateral bending). Additional information on model development and validation can be found in Campbell et al. (2016). Briefly, the FE model consisted of rigid bones and endplates, seven relevant spinal ligaments defined as nonlinear tension-only connector elements (Campbell and Petrella 2015), nucleus pulposus modeled as a nearly incompressible fluid cavity with homogeneous fluid pressure, and annulus fibrosis modeled using the Holzapfel–Gasser–Ogden (HGO) material formulation (Holzapfel et al. 2000; Gasser et al. 2005). The HGO model is an anisotropic hyperelastic material available natively in Abaqus that allows for collagen fiber angles to be defined numerically so that morphological changes in the continuum do not affect the orientation of the fiber network. The HGO strain energy potential was defined as,

$$U = C_{10}(\bar{I}_1 - 3) + \frac{1}{D} \left(\frac{(J^{el})^2 - 1}{2} - \ln J^{el} \right) + \frac{k_1}{2k_2} \sum_{\alpha=1}^N \{ \exp[k_2 \langle \bar{E}_\alpha \rangle^2] - 1 \}, \quad (1)$$

with

$$\bar{E}_\alpha = \kappa(\bar{I}_1 - 3) + (1 - 3\kappa)(\bar{I}_{4(\alpha\alpha)} - 1), \quad (2)$$

where U is the strain energy per unit of reference volume; C_{10} , D , k_1 , k_2 , and κ are temperature-dependent material parameters; N is the number of families of collagen fibers ($N = 2$); \bar{I}_1 is the first invariant of $\bar{\mathbf{C}}$ (the distortional part of the right Cauchy–Green strain tensor); J^{el} is the elastic volume ratio; and $\bar{I}_{4(\alpha\alpha)}$ are pseudo-invariants of $\bar{\mathbf{C}}$ and \mathbf{A}_α . The parameter C_{10} is equal to $\mu/2$, where μ is the shear modulus

of the annulus. D characterizes the volumetric response of the annulus and is inversely proportional to the bulk modulus. The quantity \bar{E}_α constitutes the deformation of the family of collagen fibers with mean direction \mathbf{A}_α . For perfectly aligned fibers ($\kappa = 0$), $\bar{E}_\alpha = \bar{I}_{4(\alpha\alpha)} - 1$ and for randomly distributed fibers ($\kappa = \frac{1}{3}$), $\bar{E}_\alpha = (\bar{I}_1 - 3)/3$. The annulus fibrosis properties in the present study were divided into anterior, lateral, and posterior regions (Rao 2012). The parameters C_{10} , k_1 , and k_2 were defined based on experimental findings for each region (Eberlein et al. 2001, 2004; Malandrino et al. 2013) and fiber angles were based on the average angle for each region as defined by a regression model from Holzapfel et al. (2005). The annulus material parameters were used in a sensitivity analysis and further considered in a material stiffness calibration described in Sect. 2.3.

For computational efficiency, facet cartilage was modeled using rigid hexahedral elements. Rigid contact surfaces were created for each facet pair and contact interaction was defined using frictionless softened contact with a linear pressure-overclosure relationship. The original slope ($k = 100$ MPa/mm) used to define the pressure-overclosure curve (Campbell et al. 2016) was increased in the present study by one order of magnitude ($k = 1000$ MPa/mm) to prevent excessive penetration between facet contact pairs. This change had no effect on predicted facet contact forces, it only ensured successful completion of all FE simulations across the wide range of subject-specific movement and loading patterns examined.

The number of elements for each portion of the FE model included 7470 elements for each vertebra, 2154 quadrilateral surface elements per disc to model the nucleus pulposus fluid cavity, 3108 linear hexahedral elements per disc for the annulus fibrosis, and 1200 rigid hexahedral elements for each facet cartilage pair.

2.3 Model calibration

2.3.1 Stiffness calibration

A material property calibration was employed such that the FE model would be capable of producing realistic estimates of tissue loads when driven by physiological kinematics and muscle forces. We found this particularly important in the context of the high flexion angles attained by participants in the sit-to-stand activity. Although the FE model had been previously validated at low flexion angles ($<5^\circ$), initial testing of the multiscale model revealed excessively high disc pressure and annulus stress at peak flexion angles ($\approx 60^\circ$). Based on a previous sensitivity study using a fractional factorial design of experiments (DOE) to determine the influence of intervertebral disc hyperelastic material parameters on a lumbar functional spinal unit (Honegger et al. 2019), the parameters found to have the strongest influence on all

lumbar spine responses (intradiscal pressure, axial section load, facet contact force, and intervertebral rotation) were κ , C_{10} , and D (Eqs. 1 and 2). The coefficient C_{10} is directly related to the annulus fibrosis shear modulus, which has been consistently reported ($\mu = 0.5$ MPa) (Eberlein et al. 2001, 2004). Therefore, this parameter was not changed. Parameters κ and D were selected for calibration and were manually tuned to seek reasonable agreement of FE model predictions with in vitro data for moment-rotation, disc pressure, axial force-displacement, and annulus stress reported in the literature (please see Sect. 2.4). κ was tuned from its initial value of 0 (Campbell et al. 2016) to 0.27. In addition, although annulus tissue is often assumed to be incompressible ($D = 0$), $D > 0$ can serve as a user-specified penalty parameter in the HGO model (Eberlein et al. 2001) and tuning this value allows a small amount of compressibility. Thus, the D parameter was calibrated to a value of 0.3 similar to previous studies that represented the annulus fibrosis with a hyperelastic material (Rohmann et al. 2009; Kiapour et al. 2012).

2.3.2 Rhythm calibration

The fundamental rationale of the multiscale framework was that the musculoskeletal length scale was intended to capture whole-body biomechanics with limited tissue-level detail, while the FE model was specifically included to focus on the detail of tissue-level structures. Although the musculoskeletal model was originally reported with a lumbar rhythm (Christophy et al. 2012), in light of our multiscale modeling rationale it was only sensible to employ the lumbar kinematic rhythm that naturally arose from the geometry and soft tissue structures of the FE model. The FE kinematic rhythm was, therefore, simulated using pure bending tests of 7.5 Nm (Wilke et al. 1998). The relative contribution of each intervertebral rotation to total lumbar spine (L1–L5) rotation was measured for each DOF (Fig. 1) and applied to the musculoskeletal model. The L5–S1 contribution to lumbar rotation remained unchanged from Christophy et al. (2012), as our FE model did not contain S1. Although our rhythm was different from the original, it was nevertheless in good agreement with lumbar ranges of motion and kinematic rhythms reported in the literature (Wong et al. 2006; Pearcy 1985; Fujii et al. 2007; Rozumalski et al. 2008).

2.4 Validation of tissue loads

Following calibration of the FE model intervertebral stiffness properties, preliminary validation of the lumbar spine moment-rotation and force-displacement response was conducted to ensure appropriate model predictions prior to running full simulations of the multiscale modeling framework. The moment-rotation response of the updated FE model was

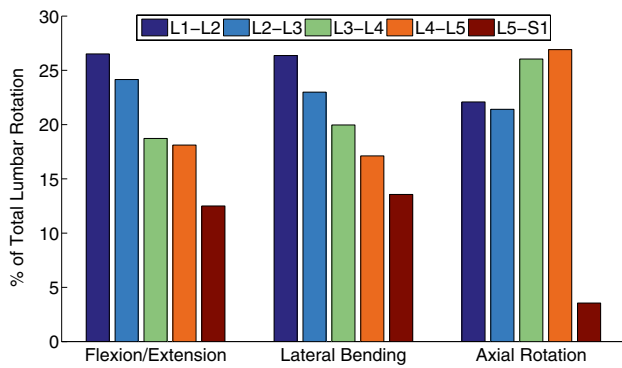


Fig. 1 Lumbar spine rhythm used in the multiscale model. The L1–L5 values were calculated from the FE model pure bending simulations of 7.5 Nm. L5–S1 rhythm values remained unchanged from Christophy et al. (2012)

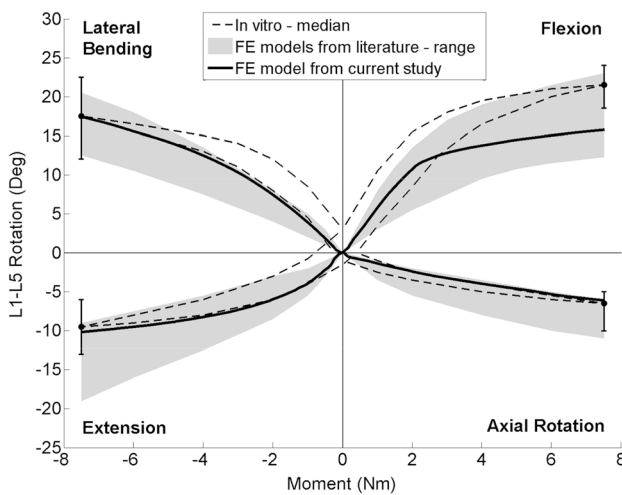


Fig. 2 Moment-rotation response validation comparing the L1–L5 results from the calibrated FE model to in vitro values from Rohlmann et al. (2001). The error bars indicate the range of in vitro values at 7.5 Nm. The shaded area defines the range of moment-rotation responses from the 8 FE models investigated in Dreischarf et al. (2014) which are Ayturk and Puttlitz (2011); Kiapour et al. (2012); Little et al. (2008); Liu et al. (2011); Park et al. (2013); Schmidt et al. (2012); Shirazi-Adl (1994); Zander et al. (2009)

compared to the median response of reported in vitro data from ten lumbar spines (Rohlmann et al. 2001) and the range of responses from eight published FE models of the lumbar spine (Dreischarf et al. 2014; Ayturk and Puttlitz 2011; Kiapour et al. 2012; Little et al. 2008; Liu et al. 2011; Park et al. 2013; Schmidt et al. 2012; Shirazi-Adl 1994; Zander et al. 2009) by applying pure bending moments of 7.5 Nm in flexion, extension, lateral bending, and axial rotation Wilke et al. (1998) to the L1–L5 spine (Fig. 2). The rotational stiffness values for the lumbar spine bushings in the musculoskeletal model were subsequently updated from their original values defined in Senteler et al. (2016) with the new

Table 1 Intervertebral stiffness values for all 3 rotational degrees of freedom for lumbar spine levels L1–L5 computed by the FE model in isolated moment-rotation simulations

Lumbar level	Rotational stiffness (Nm/rad)		
	Flexion/extension (K_{RZ})	Lateral bending (K_{RX})	Axial rotation (K_{RY})
L1-L2	39	51	128
L2-L3	45	63	183
L3-L4	66	64	187
L4-L5	72	72	185

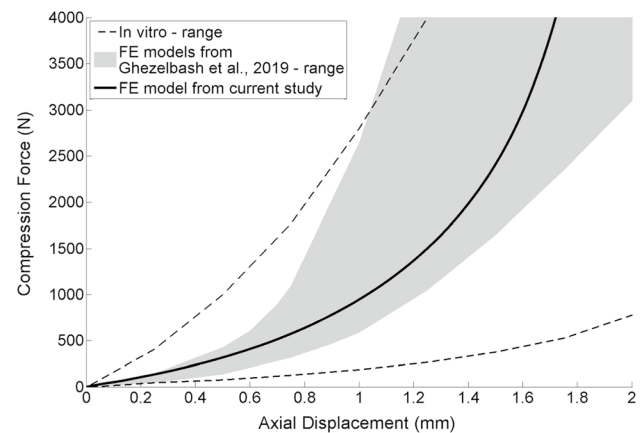


Fig. 3 Force-displacement response validation comparing L2–L3 results from the calibrated FE model to in vitro values from Brown et al. (1957); Markolf and Morris (1974); Tencer et al. (1982); Asano et al. (1992); Jamison et al. (2013); Marini et al. (2016) as well as the range of responses from the FE models in Ghezelbash et al. (2019b)

linear stiffness values calculated from the moment-rotation response of the FE model (Table 1).

The force-displacement response of the L2–L3 FE intervertebral disc under uniform axial compression was compared to a range of responses from in vitro data (Brown et al. 1957; Markolf and Morris 1974; Tencer et al. 1982; Asano et al. 1992; Jamison et al. 2013; Marini et al. 2016) as well as a range of responses from the FE models in Ghezelbash et al. (2019b) (Fig. 3). The intradiscal pressure response of the L4–L5 intervertebral disc under compression was compared to in vitro data from 15 lumbar spine segments (Brinckmann and Grootenboer 1991) and, again, to the range of model responses from the FE models in Ghezelbash et al. (2019b) (Fig. 4).

In consideration of the calibrated FE model responses falling within the range of moment-rotation, disc pressure, and force-displacement responses reported by previous in vitro and FE modeling studies (Figs. 2, 3, and 4), the FE

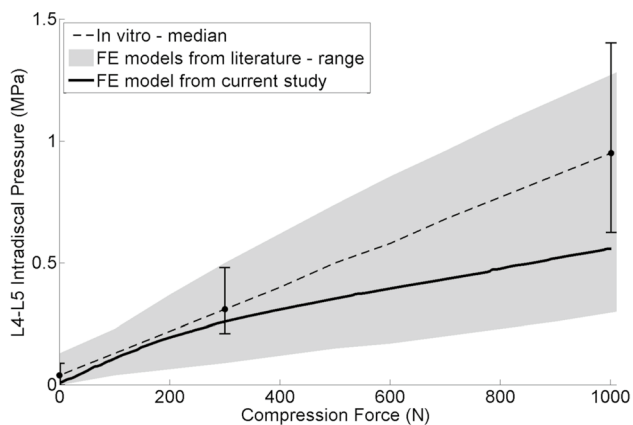


Fig. 4 Intradiscal pressure response validation comparing L4–L5 results from the calibrated FE model to in vitro values from Brinckmann and Grootenboer (1991) and the range of FE model responses investigated in Dreischarf et al. (2014) which include Ayturk and Puttlitz (2011); Kiapour et al. (2012); Little et al. (2008); Liu et al. (2011); Park et al. (2013); Schmidt et al. (2012); Shirazi-Adl (1994); Zander et al. (2009). The error bars indicate the range of in vitro values at 0 N, 300 N, and 1000 N, respectively

model was deemed credible for inclusion in the multiscale modeling workflow.

2.5 Multiscale model

The FE geometry was scaled uniformly to each participant based on torso length (Fig. 5.1) and registered to the nominal configuration of the lumbar spine musculoskeletal model in the global reference frame using an Iterative Closest Point algorithm (Bergström 2006) (Fig. 5.2). Intervertebral bushing locations were also adjusted to match the scaled joint locations calculated by the OpenSim scaling tool. Lumbar spine muscle attachment locations were obtained from the musculoskeletal model (van Arkel et al. 2013; Phillips et al. 2015) and transferred to the FE model for application of muscle forces (Fig. 5.4). Connector elements were defined in Abaqus at each intervertebral level to control relative rotation of adjacent vertebrae, and 3-DOF rotational kinematics from the musculoskeletal model were applied as inputs to the FE model. Translational DOFs at each intervertebral

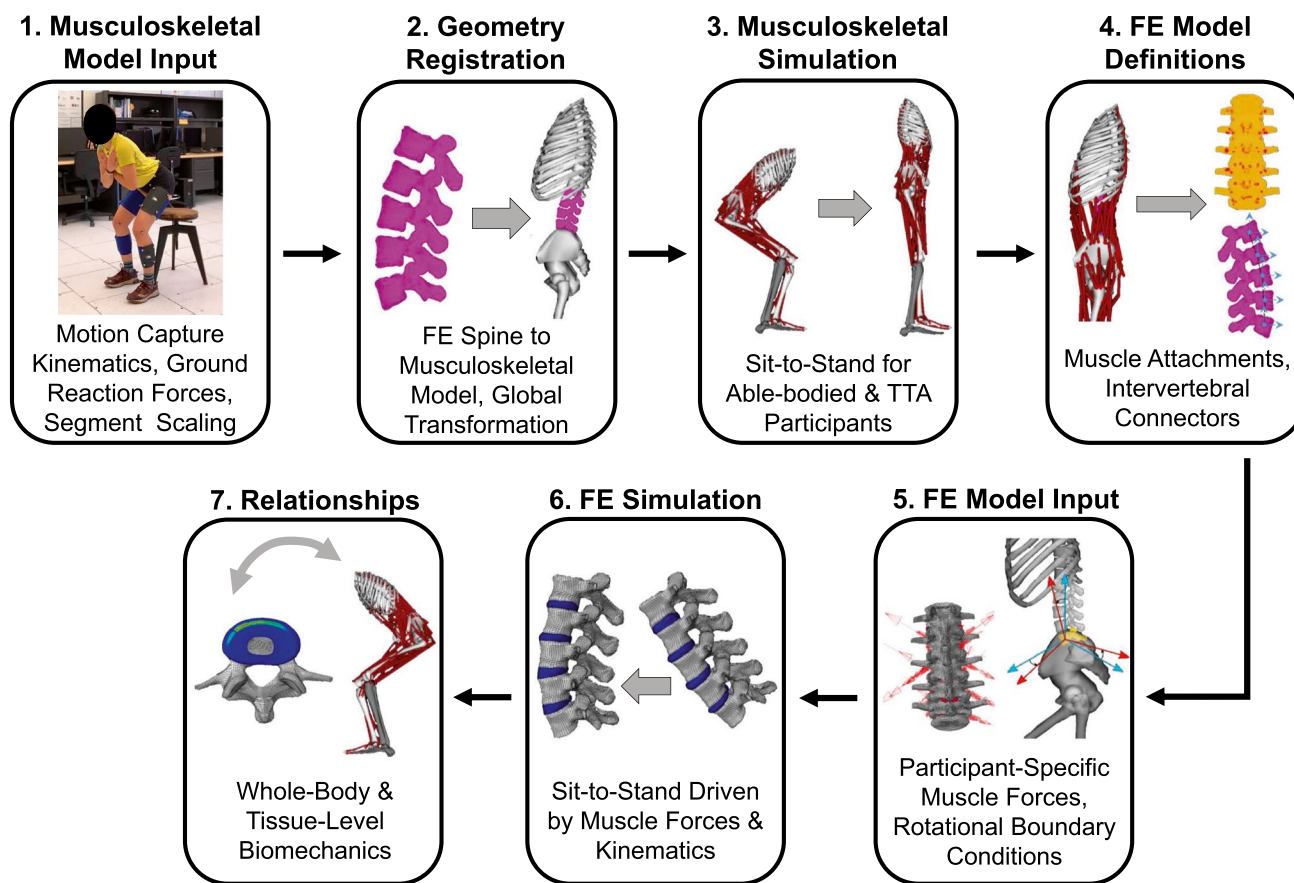


Fig. 5 Multiscale model workflow: (1) Experimental data collection on participants performing sit-to-stand; (2) lumbar spine geometry registration; (3) sit-to-stand simulation of the musculoskeletal model; (4) muscle attachment locations and intervertebral rotational connector definitions; (5) prescription of joint angles, boundary conditions,

muscle forces, and joint contact forces; (6) FE simulation; (7) determination of whole-body and tissue-level relationships between lumbar spine rotations and annulus fibrosis stress, intradiscal pressure, and facet contact force

level remained free in the FE model to enable realistic spinal motion and load transfer.

2.6 Experimental protocol

Eight people, four able-bodied (1 male, 3 females, 23.3 ± 2.9 years, 1.66 ± 0.06 m, 65.9 ± 9.3 kg) and four with a unilateral TTA (4 males, 45.5 ± 14.8 years, 1.84 ± 0.02 m, 99.4 ± 15.3 kg), provided written informed consent to participate in the institutionally-approved experimental protocol. No participant had more than minimal LBP as indicated by the Modified Oswestry Low Back Pain Questionnaire (Fairbank and Pynsent 2000) (able-bodied: $0 \pm 0\%$, TTA: $2.5 \pm 3\%$).

All participants performed five self-paced sit-to-stand trials, starting from seated with hips, knees, and ankles at 90° of flexion and feet hip-width apart on separate force plates (1200 Hz, AMTI Inc., Watertown, MA) (Fig. 5.1) Participants were instructed to keep arms folded across the chest for the duration of the trial. Kinematics were collected at 120 Hz using a 20-camera motion capture system (Motion Analysis Corp., Santa Rosa, CA) and a full-body marker set including reflective markers placed at C7, T8, sternal notch, xiphoid process, and bilaterally at the acromion, posterior superior iliac spine, anterior superior iliac spine, iliac crest, greater trochanter, 4-marker thigh cluster, medial/lateral femoral condyles, 4-marker shank cluster, medial/lateral malleoli, heel, 1st metatarsal head and 5th metatarsal head.

2.7 Multiscale simulation workflow

Motion capture kinematics and ground reaction forces (GRFs) were low-pass filtered with a bi-directional 4th-order Butterworth filter with cutoff frequencies of 6 and 10 Hz, respectively. Participant-specific uniform segment scale factors were determined, and the inverse kinematics solution was computed using a least-squares optimization algorithm (Lu and O'Connor 1999) in Visual3D (C-Motion, Inc., Germantown, MD). Uniform scale factors were input into the OpenSim scaling tool and applied to the generic musculoskeletal model. The duration of sit-to-stand extracted for use with the multiscale model was defined as the moment of lift-off from the chair to upright standing. The instant of lift-off was determined as in Actis et al. (2018b). Termination of trunk center-of-mass velocity defined upright standing. The inverse kinematics solution and GRFs for the sit-to-stand duration were then input to the residual reduction algorithm (RRA) in OpenSim to reduce residual forces and moments at the pelvis, improving dynamic consistency (Fig. 5.3). A static optimization algorithm using interior point optimization (Wächter and Biegler 2006) was performed to resolve the net joint torques from RRA into individual muscle forces at each time step, by minimizing the objective function (Herzog 1987):

$$J = \sum_{m=1}^{294} (a_m)^2, \quad (3)$$

subject to the following constraints, for $j = 1 : k$:

$$\sum_{m=1}^n [a_m f(F_m^0, l_m, v_m)] r_{mj} = \tau_j, \quad (4)$$

where a_m refers to the activation of muscle m , f is the maximum force of the muscle as a function of its maximum isometric force (F_m^0), length (l_m), and velocity (v_m), r_{mj} is the moment arm of muscle m about joint j , n is the number of muscles spanning joint j , k is the total number of joints in the model, and τ_j is the net joint torque at joint j . Detail on the theory and implementation of the muscle model used for the 294 musculotendon actuators, which is based on the Hill-type muscle model (Hill 1938), can be found in the Appendix section of Thelen (2003).

The maximum isometric force of each trunk muscle was systematically increased by 10% for models that failed during the static optimization procedure. This increase was to ensure that the model was using muscles and not additional reserve torque actuation to reproduce the experimentally-measured motion. The muscles were incrementally scaled until the solver was able to find a solution at all time points of the corresponding trial. The means and standard deviations of the trunk maximum isometric force scale factors for able-bodied participants and participants with TTA were 1.23 ± 0.18 and 2.27 ± 0.77 , respectively. Similarly, other musculoskeletal modeling studies have increased the maximum isometric forces of trunk muscles to ensure sufficient muscle strength for different dynamic simulations of movement (Raabe and Chaudhari 2016; Beaucage-Gauvreau et al. 2019).

Muscle forces for all trunk muscle fascicles were combined into relevant groups and summed for each sit-to-stand trial. The muscle groups and their corresponding muscle fascicles were: erector spinae (longissimus thoracis pars thoracis, longissimus thoracis pars lumborum, iliocostalis lumborum pars thoracis, and iliocostalis lumborum pars lumborum); psoas major; multifidus; rectus abdominis; obliques (internal and external obliques); and quadratus lumborum. Averages were computed for each participant over 5 trials and then for each participant group.

Intervertebral joint angles resulting from application of the lumbar kinematic rhythm in OpenSim were applied to the FE model (Fig. 5.5). A custom OpenSim plugin (van Arkel et al. 2013; Phillips et al. 2015) (simtk.org) was used to obtain the muscle force unit vectors and magnitudes for each lumbar spine muscle and then applied to the FE model as loading conditions (Fig. 5.5–6). Joint contact forces and moments were also extracted for the joint between the torso

and L1 in the musculoskeletal model and applied to the FE model for dynamic consistency (Fig. 5.5–6).

2.8 Output statistical analysis

To quantify bilateral symmetry and capture potential biomechanical differences between amputated vs. intact limbs (among participants with TTA) and dominant vs. non-dominant (among able-bodied participants), a symmetry index of vertical ground reaction force (vGRF) was calculated (Burnett et al. 2011):

$$SI = \frac{\text{Peak vGRF}_{(R,ND)}}{\text{Peak vGRF}_{(I,D)}} \quad (5)$$

where the symmetry index (*SI*) for a single trial is calculated by dividing the peak vGRF for the residual (*R*) limb (or non-dominant (*ND*) limb) by the peak vGRF for the intact (*I*) limb (or dominant (*D*) limb).

Trunk-pelvis rotations in the three anatomical planes (sagittal, frontal, and transverse), spinal muscle forces, and net L4–L5 joint contact loads for each sit-to-stand trial were extracted from the musculoskeletal simulations for comparison. To focus on one relevant level for comparison to in vivo data (Wilke et al. 2001), tissue-level load transfer metrics were extracted from only the L4–L5 level. The tissue-level metrics selected for output from the FE simulations were annulus fibrosis von Mises (vM) stress (peak value), facet contact forces, and nucleus pulposus fluid cavity pressure. Annulus stress results were extracted from the posterior region as this is the location known for damage to initiate and propagate (Shahraki et al. 2015) and known to exhibit high stresses that correlate with pain (McNally et al. 1996; Bogduk 2012). Facet contact forces at each level were calculated by summing the values from the right and left sides of the anatomy.

A total of 40 sit-to-stand trials were simulated for the eight participants. Although trial duration varied (0.82–1.79 s), output curves were normalized by extracting results at 100 evenly-spaced time points for each trial. The range and maximum value were identified for each curve; these were then averaged over the five trials for each participant and pooled by participant group (referred to below as RNG (range) and MAX (maximum value)). Complete output curves were also averaged over all trials for each participant and average curves were pooled by group (referred to below as TOT (total curve)). Comparisons were made between participant groups with and without TTA using t-tests ($\alpha=0.05$). Effect size was calculated for each t-test using Cohen's *d* (Cohen 1992).

To determine if tissue-level loading could be reliably predicted from lumbar rotations alone without the need for a multiscale model, we plotted the participant average

curves for each tissue-level outcome metric versus each lumbar spine rotation to look for trends (Fig. 5.7).

2.9 Intradiscal pressure comparison

Out of the range of tasks analyzed in previous studies that measured in vivo L4–L5 intradiscal pressure (IDP) (Nachemson 1965; Wilke et al. 1999; Sato et al. 1999; Wilke et al. 2001), only Wilke et al. (2001) measured IDP during the task of standing up from a chair. The study only reports the peak pressure value during sit-to-stand for a single participant. For validation of multiscale IDP estimates, we compared our predictions from all participants to the peak IDP during sit-to-stand reported in Wilke et al. (2001). L4–L5 IDP estimates from the multiscale model comprised direct pressure results from the FE model and axial L4–L5 joint contact loads from OpenSim that were converted to IDP using two conversion equations. The first equation is from Dreischarf et al. (2013),

$$IDP = \frac{F_C}{CSA \times 0.66} \quad (6)$$

and the second expression is from Ghezalbash et al. (2016),

$$IDP(P, \theta) = -1.556 \times 10^{-2} + 1.255P + 1.243 \times 10^{-2}\theta + 3.988 \times 10^{-2}P^2 - 1.212 \times 10^{-2}P\theta + 1.669 \times 10^{-3}\theta^2, \quad (7)$$

where F_C is the axial compressive force, CSA is the disc cross-sectional area, 0.66 is a correction factor for conversion between IDP and compressive loading (Nachemson 1960; Dreischarf et al. 2013), P (MPa) is the nominal pressure (F_C/CSA) and θ ($^\circ$) is the L4–L5 intersegmental flexion angle. The intervertebral disc CSA was defined as 18 cm², reported by Wilke et al. (2001). Comparisons of L4–L5 IDP normalized to the upright standing value (taken as the final data point in our sit-to-stand simulation) as well as comparisons of absolute values of L4–L5 IDP were made.

3 Results

Both the musculoskeletal and FE simulations completed successfully for all 40 sit-to-stand trials. Average root-mean-squared (RMS) residual forces and moments in the musculoskeletal model across all participants and all trials were small, indicating credible results (0.94, 0.41, 0.88 %BW forces in the anterior/posterior, superior/inferior, and medial/lateral directions, and 0.36, 0.21, and 2.60 %BW-m moments in the frontal, transverse, and sagittal planes).

3.1 Kinematics

Values of trunk-pelvis range of motion in the sagittal, frontal, and transverse planes were not different between groups (Fig. 6, *t* tests not shown). However, the comparison of average curves pooled by group (TOT) revealed that average trunk-pelvis angles over the sit-to-stand motion were greater for participants with TTA compared to able-bodied participants in all planes ($p < 0.001$) (Table 2). The maximum values for axial rotation (i.e., toward the intact or dominant limb) were greater in participants with TTA ($p = 0.029$) and the minimum values for axial rotation (i.e., toward the non-dominant or residual limb) were greater in able-bodied participants ($p = 0.017$) (Table 2). In addition, the greatest differences in trunk-pelvis kinematics between participants with and without TTA occurred at the moment of lift-off, in which participants with TTA were an average of 12.8^{circ} more flexed and 2.5^{circ} more axially rotated (Fig. 6).

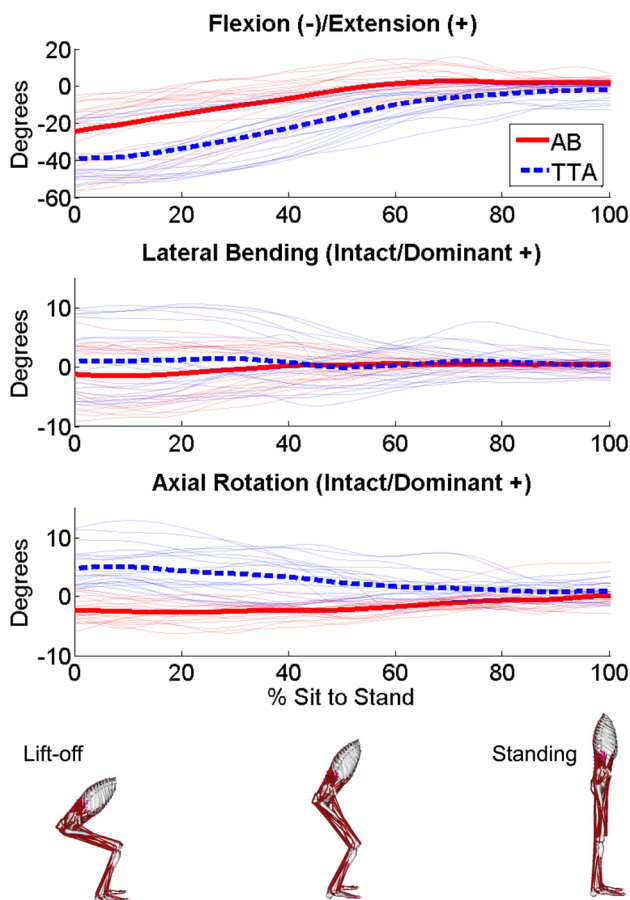


Fig. 6 Trunk-pelvis kinematics (mean) for participants with (TTA) and without (AB) a transtibial amputation (solid and dashed curves). Kinematics for individual trials are shown as light red lines for able-bodied participants and light blue lines for participants with TTA

3.2 Symmetry index

Participants with TTA had a smaller symmetry index ($SI = 0.83$) compared with able-bodied participants ($SI = 1.00$) ($p < 0.001$) (Table 2). These values indicate favoring of the intact limb for participants with TTA while able-bodied participants remained more symmetric (Equation 5).

3.3 Muscle forces

Average values of trunk muscle forces over the sit-to-stand cycle (TOT) were greater among participants with TTA compared to able-bodied participants ($p < 0.05$) for all muscle groups (Fig. 7, Table 2). The range of erector spinae muscle forces approached being significantly greater for able-bodied participants compared to participants with TTA ($p = 0.081$). The ranges of rectus abdominis and quadratus lumborum muscle forces were greater for participants with TTA compared to participants without ($p < 0.05$) (Table 2). The maximum rectus abdominis and quadratus lumborum muscle forces were also greater for participants with TTA ($p < 0.001$) (Fig. 7, Table 2). Average values for rectus abdominis and quadratus lumborum muscle forces throughout sit-to-stand (TOT) were 0.07 and 0.47 BW, respectively, for participants with TTA, while able-bodied participant averages were much lower (0.04 and 0.03 BW, respectively) (Table 2).

3.4 Net joint contact loads

Net compressive and shear L4–L5 joint contact loads were greater on average (TOT) in participants with TTA compared to able-bodied participants ($p < 0.05$) (Table 2). Average force values were 2.63 and 1.77 BW in compression and 0.76 and 0.56 BW in shear for participants with and without TTA, respectively. In addition, the maximum compressive L4–L5 load was greater for participants with TTA (4.29 BW) compared with able-bodied participants (3.12 BW) ($p = 0.042$) (Table 2).

3.5 Tissue-level mechanics

For all tissue-level load transfer metrics investigated (annulus fibrosis vM stress, facet contact force, and intradiscal pressure), average values over the sit-to-stand cycle (TOT) were greater for participants with TTA compared with able-bodied participants (Table 2). The range of L4–L5 facet contact forces approached being significantly greater for participants with TTA (508 N) compared to able-bodied participants (279 N) ($p = 0.054$) (Table 2). The maximum values for facet contact force and intradiscal pressure also approached being significantly greater for participants with

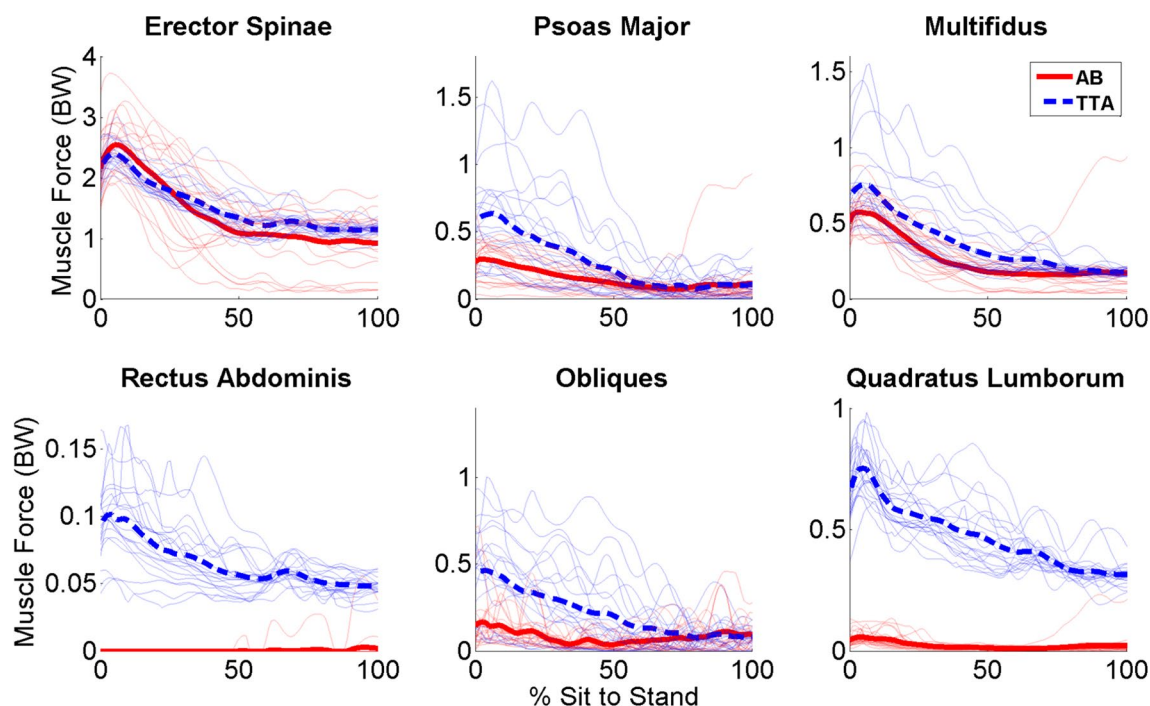


Fig. 7 Summed trunk and abdominal muscle forces per body-weight (erector spinae: longissimus thoracis pars thoracis, longissimus thoracis pars lumborum, iliocostalis lumborum pars thoracis, and iliocostalis lumborum pars lumborum; psoas major; multifidus; rectus abdominis; obliques: internal and external obliques; and quad-

ratus lumborum) (mean values) for able-bodied participants (solid red lines) and participants with TTA (dashed blue lines). Individual force sums for each sit-to-stand trial are shown as light red lines for able-bodied participants and light blue lines for participants with TTA

TTA (mean values of 513 N and 3.96 MPa, respectively) compared to able-bodied participants (mean values of 282 N and 2.81 MPa, respectively) (Table 2).

3.6 Kinematic and load relationships

Relationships between tissue-level load transfer metrics and lumbar rotations (Fig. 8) generally indicated that annulus fibrosis stress and IDP were highest shortly after lift-off when all three lumbar rotations deviated to the greatest extent from their zero values (referenced to a nominal standing posture). Facet forces had the opposite trend, with higher force values predicted when lumbar rotations were near zero and away from a flexed position. Other clear trends in variation of tissue loads with spinal motion were not visually obvious, highlighting what appeared to be strongly individual patterns of loading and motion during the sit-to-stand task.

3.7 Annulus fibrosis stress

The annulus vM stress peak moved about the posterior portion of the annulus for each participant in a manner that consistently tracked with individual kinematics. The overall peak stress occurred in the inner postero-lateral region of

the disc just after lift-off at the moment of maximum flexion and/or lateral bending (Fig. 9). The stress peak then moved to the mid-sagittal plane as participants became less flexed and bent laterally, and it continued decreasing until the end of the sit-to-stand cycle (Figs. 8, 9). Some participants without TTA maintained very symmetric motion during the sit-to-stand task, but for any participant who bent laterally while rising from the chair, the overall peak annulus stress was always on the side to which the individual was leaning.

3.8 Intradiscal pressure comparisons

Results for IDP from the musculoskeletal model normalized to upright standing were in good agreement with Wilke et al. (2001) for both participant groups (Fig. 10). Normalized IDP estimates from the FE model for participants with TTA also fell within the range of the previously reported data, but FE results for the able-bodied participants were slightly higher than Wilke et al. (2001). Comparing absolute values of L4–L5 IDP during upright standing, only the range of musculoskeletal model estimates for able-bodied participants using the conversion equation from Ghezlbash et al. (2016) (0.42–0.76 MPa) were close to the value reported by Wilke et al. (2001) (0.5 MPa) (Fig. 10). The IDP estimates for able-bodied participants from the musculoskeletal model

Table 2 Summary of group mean (\pm SD) of outcome metrics that were significantly different ($p < 0.05$, *) or approached significance ($0.05 \leq p \leq 0.1$, ~). Measures include range of values (RNG), maximum values (MAX), minimum values (MIN), and the overall average of values (TOT), where (D/I) and (N/R) refer to dominant/intact and non-dominant/residual limb, respectively

Metric	DOF, Group, or Location	Measure	TTA	Able-bodied	Effect size	<i>p</i> value	
Symmetry index	Vertical GRF	N/A	0.83 (0.11)	1.00 (0.1)	1.647	0.000*	
Trunk-pelvis angle (°)	Flexion (-)/ Extension (+)	TOT	-18.3 (16.5)	-5.93 (12.8)	0.842	0.000*	
		Lateral bending	TOT	0.76 (3.77)	-0.10 (3.04)	-0.251	0.000*
		Axial Rotation	MAX (D/I)	5.75 (3.45)	0.67 (0.92)	-2.010	0.029*
			MIN (N/R)	-0.40 (1.38)	-3.65 (1.41)	-2.329	0.017*
Muscle force (BW)	Erector Spinae	TOT	2.74 (2.97)	-1.62 (1.45)	-1.862	0.000*	
		RNG	1.41 (0.08)	1.83 (0.39)	1.481	0.081 ~	
		TOT	1.52 (0.42)	1.41 (0.70)	-0.190	0.007*	
		Psoas Major	TOT	0.27 (0.27)	0.15 (0.10)	-0.580	0.000*
			Multifidus	TOT	0.37 (0.23)	0.27 (0.16)	-0.493
		Rectus Abdominis	RNG	0.06 (0.03)	3E-3 (6E-3)	-2.867	0.007*
	MAX		0.11 (0.03)	3E-3 (7E-3)	-4.881	0.000*	
	TOT		0.07 (0.02)	6E-4 (2E-3)	-4.163	0.000*	
	Obliques		TOT	0.22 (0.20)	0.09 (0.05)	-0.924	0.000*
			Quadratus	RNG	0.50 (0.02)	0.08 (0.03)	-15.06
	Lumborum		MAX	0.79 (0.04)	0.09 (0.03)	-19.50	0.000*
	Net joint loading (BW)	L4-L5 Compression	TOT	0.47 (0.14)	0.03 (0.02)	-4.542	0.000*
MAX			4.29 (0.73)	3.12 (0.54)	-1.822	0.042*	
L4-L5 A/P Shear		TOT	2.63 (0.83)	1.77 (0.71)	-1.113	0.000*	
		TOT	0.76 (0.22)	0.56 (0.26)	-0.814	0.000*	
Annulus fibrosis von mises stress (MPa)	L4-L5 Posterior, Peak	TOT	4.82 (2.54)	2.99 (1.99)	-0.805	0.000*	
Facet contact force (N)	L4-L5	RNG	508 (38.0)	279 (188)	-1.687	0.054 ~	
		MAX	513 (39.4)	282 (191)	-1.673	0.056 ~	
		TOT	138 (116)	37.7 (49.2)	-1.126	0.000*	
Intradiscal pressure (MPa)	L4-L5	MAX	3.96 (0.93)	2.81 (0.58)	-1.484	0.081 ~	
		TOT	2.13 (0.96)	1.39 (0.75)	-0.867	0.000*	

using the Dreischarf et al. (2013) conversion equation (lower bound = 0.53 MPa) and from the FE model (lower bound = 0.52 MPa) were close to the in vivo results. All estimates of absolute IDP during upright standing for participants with TTA were greater than the value reported in Wilke et al. (2001) (Fig. 10).

One able-bodied participant from our study (height = 175 cm, weight = 70 kg), denoted as AB1, matched the anthropometry of the participant in Wilke et al. (2001) (height = 174 cm, weight = 72 kg). Thus, this participant's resulting L4-L5 IDP was also compared separately. Model estimates for IDP during upright standing were close in magnitude to the in vivo value reported in Wilke et al. (2001) (0.5 MPa) (Fig. 11). However, estimates for peak IDP during sit-to-stand all over-estimated the value from Wilke et al. (2001) (Fig. 11). The peak IDP averaged across all AB1 trials for the musculoskeletal model using the Dreischarf et al. (2013) conversion factor, the musculoskeletal model using the Ghezalbash et al. (2016) conversion factor, and the FE

model were 1.5, 1.3, and 2.1 MPa, respectively compared to 1.1 MPa reported in Wilke et al. (2001).

4 Discussion

A multiscale model of the lumbar spine was developed for people with and without TTA to investigate loads within the tissue structures of the lumbar spine during sit-to-stand and to determine if there is a relationship between an individual's lumbar spine kinematics and the resulting tissue loads. To the best of our knowledge, this was the first study to use a multiscale modeling framework to estimate lumbar spine tissue loads for two distinct population groups while simulating a dynamic activity of daily living. The multiscale model was robust to changes in participant characteristics and model inputs, successfully simulating all 40 trials. The model provided insight into participant-specific lumbar spine kinematics and the

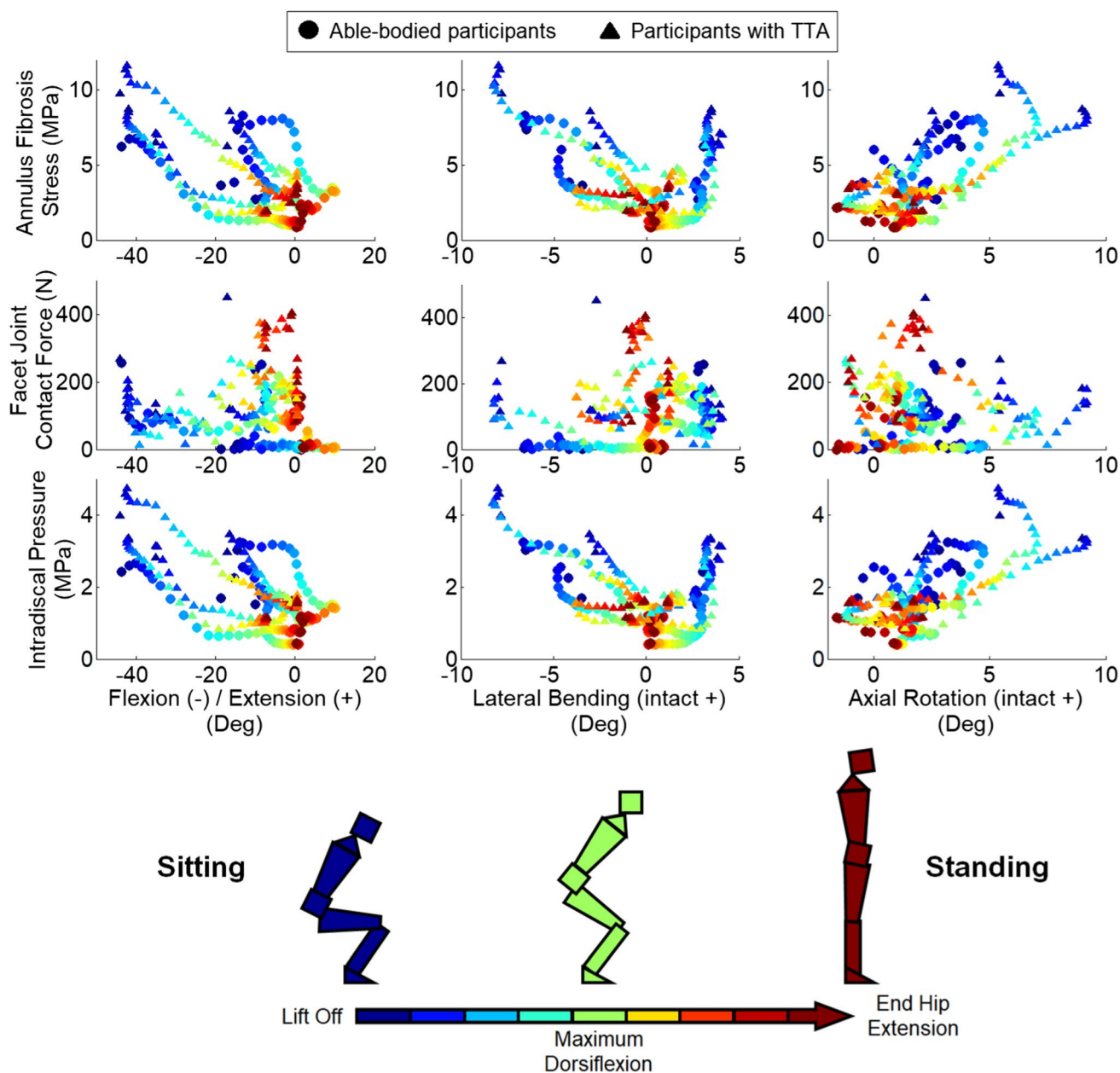


Fig. 8 L4–L5 tissue-level load transfer metrics (annulus fibrosis stress, facet joint contact force, and intradiscal pressure) versus lumbar spine rotations (flexion/extension, lateral bending, and axial rotation) for participants with a transtibial amputation (TTA) and able-

bodied participants (AB) (average participant curves). Temperature color-map (cold to warm) signifies progression from lift-off to standing

magnitude, timing, and distribution of tissue-level load transfer, which answered our first question: What loads develop within the tissue structures of the lumbar spine for individuals with and without TTA during sit-to-stand? With the exclusion of trunk-pelvis ranges of motion, our results did follow our expectations that participants with TTA would exhibit greater trunk muscle forces, net joint loads, and tissue-level loads compared with able-bodied participants (Fig. 7, Table 2).

Participants with TTA adopted a more flexed posture and rotated their trunk toward the intact limb as opposed to able-bodied participants who flexed less and generally maintained a more neutral posture throughout sit-to-stand (Fig. 6). While all participants with TTA rotated toward their intact versus amputated limb, some bent laterally toward their intact limb while others bent toward their amputated side (Figs. 6, 8). This finding demonstrates differences between participants even within a specific subpopulation

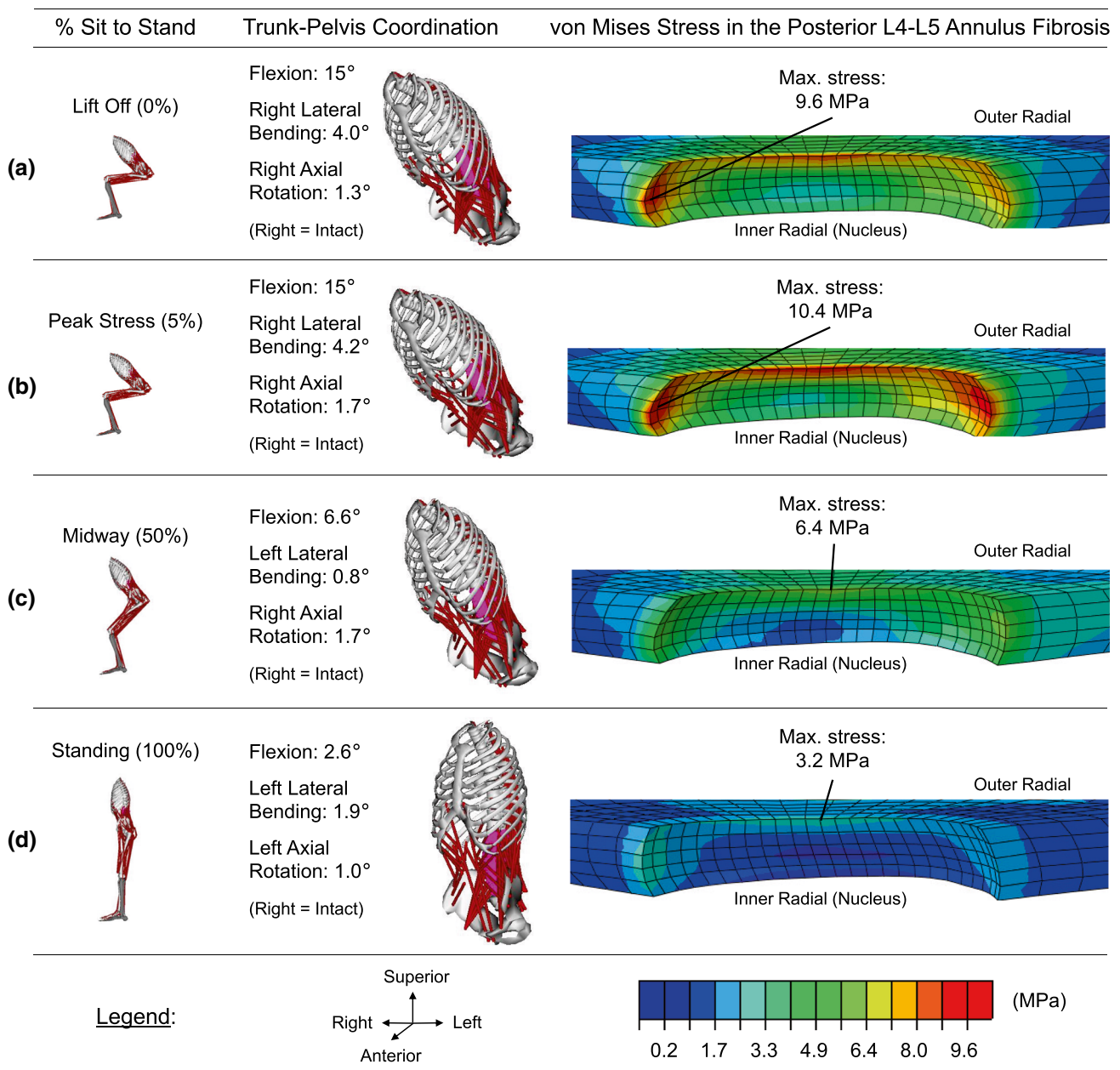


Fig. 9 Example of von Mises stress field distribution in the posterior region of the L4–L5 annulus fibrosis for a participant with a left TTA. **a** High stress initiates in the inner right postero-lateral region at the moment of lift-off and peak flexion, **b** moment of highest stress in the

annulus coinciding with peak lateral bending, **c** stress decreases and maximum stress moves to mid-sagittal plane midway through the sit-to-stand cycle, and **d** overall and maximum stress decreases further when standing at the end of the cycle

and highlights the importance of participant-specific analysis. Nonetheless, the average symmetry index of peak vGRF for participants with TTA was 0.83 as opposed to 1.00 for able-bodied participants ($p < 0.001$) (Table 2), indicating that participants favored loading their intact limb while able-bodied participants remained more symmetric during sit-to-stand. These results suggest that people with TTA favor loading their intact limb by shifting the trunk and pelvis center-of-mass toward the intact limb when performing

sit-to-stand, which is consistent with greater GRF generation under the intact limb and in agreement with movement strategies for people with a lower-limb amputation during sitting and standing movements (Burger et al. 2005; Šljajpah et al. 2013; Hendershot and Wolf 2015).

Over the sit-to-stand motion, the average magnitudes of trunk muscle force for all muscle groups were greater for participants with TTA compared to able-bodied participants (Table 2, Fig. 7). All measures for rectus abdominis

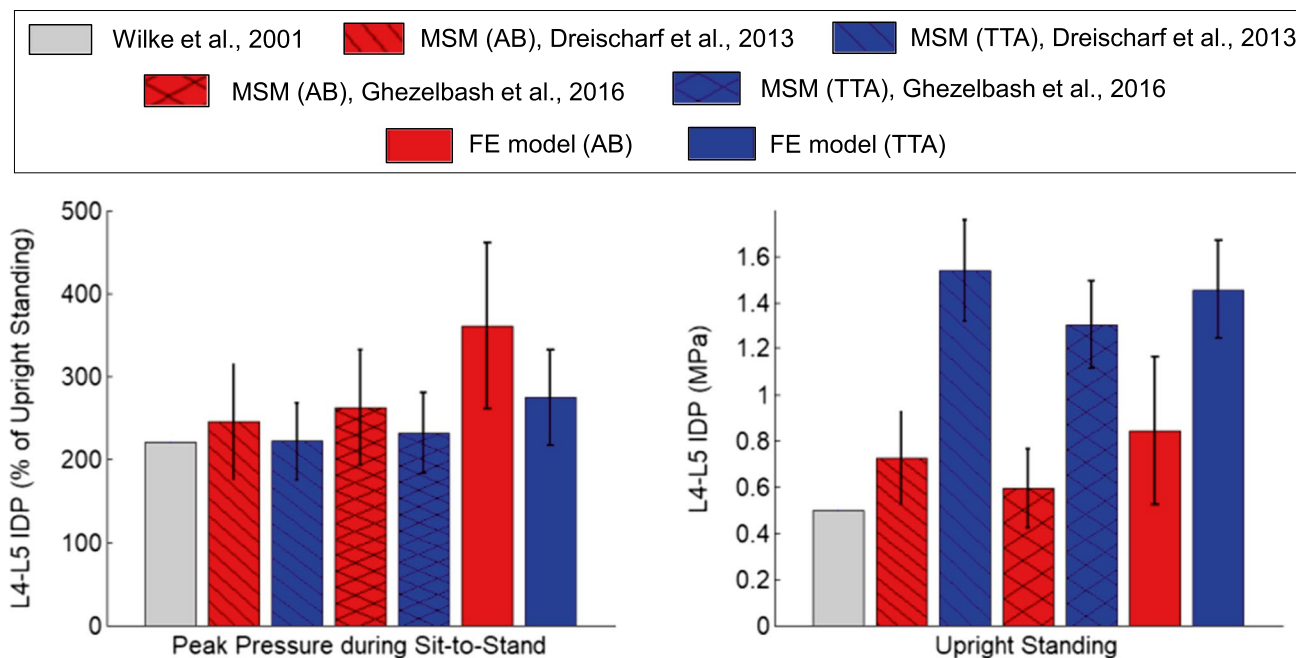


Fig. 10 Normalized and absolute L4–L5 intradiscal pressure (IDP) comparison of model estimates for able-bodied participants (red bars) and participants with TTA (blue bars) to in vivo values from the literature (Wilke et al. 2001) (gray bars). Diagonal hatch marks are designated for axial joint contact loads from the musculoskeletal model

(MSM) converted to IDP using the equation from Dreischarf et al. (2013) and crossed hatch marks are designated for axial joint contact loads converted using the equation from Ghezelbash et al. (2016). Error bars indicate ± 1 standard deviation

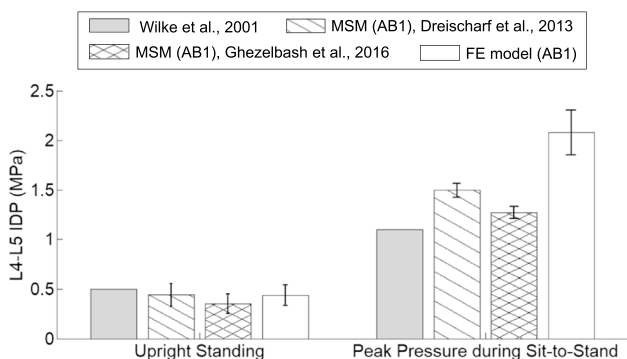


Fig. 11 L4–L5 intradiscal pressure (IDP) comparison of in vivo values and model estimates for the participant measurements from Wilke et al. (2001) (gray bars) and the five trials for the matched able-bodied participant in this study (AB1, white bars), respectively. Diagonal hatch marks are designated for axial joint contact loads from the musculoskeletal model (MSM) converted to IDP using the equation from Dreischarf et al. (2013) and crossed hatch marks are designated for axial joint contact loads converted using the equation from Ghezelbash et al. (2016)

and quadratus lumborum muscle forces that were analyzed for significance were greater for participants with TTA (Table 2). Muscle forces for both rectus abdominis and quadratus lumborum groups were active throughout sit-to-stand for participants with TTA while essentially inactive

for able-bodied participants (Fig. 7). The greater abdominal muscle activity in participants with TTA could be attributed to stabilization of the spine (Gardner-Morse and Stokes 1998). In addition, efforts to increase the stability of the spine may be a mechanism to reduce injury risk during tasks that are not demanding (Cholewicki and McGill 1996).

Average net compressive and shear L4–L5 joint contact loads were greater in participants with TTA compared to able-bodied participants, which led to greater average annulus stress, facet contact forces, and intradiscal pressure values throughout the sit-to-stand movement (Table 2). Similarly, previous work has shown that people with TTA have greater peak and average L4–L5 compressive loads during sit-to-stand compared to able-bodied participants (Actis et al. 2018b). In addition, a general trend across all participants was greater disc loading at the initiation of sit-to-stand and greater facet loading at the end of sit-to-stand (Fig. 8). This trend is consistent with the lumbar spine transitioning from greater flexion early in the motion back to a nominal posture at the end of the sit-to-stand cycle (Fig. 6). Greater ranges and peak values of facet contact force were predicted for participants with TTA during sit-to-stand in this study (Fig. 8, Table 2), which was associated with greater trunk muscle forces (Fig. 7) leading to greater facet compression. This increased compression is an important observation, as axial compression coupled with lateral bending and flexion

has been shown to lead to intervertebral disc injury (Marras et al. 1993; Adams et al. 1994, 2000; Callaghan and McGill 2001), which has potential implications for the development of LBP caused by internal disc disruption or herniation (Bogduk 2012). In addition, participants with TTA had higher peak IDP compared with able-bodied participants, but peak annulus fibrosis stress was not different between groups (Table 2). This finding highlights the unique capability of the multiscale model to quantify the distribution of tissue-level load transfer within different portions of the disc and surrounding tissues during a realistic activity of daily living. Differences in intervertebral disc load transmission between participant groups is attributed to the combination of greater back muscle activity and greater flexion (Fig. 6) observed in participants with TTA, factors that have also been correlated with greater intradiscal pressure (Andersson et al. 1977; Örtengren et al. 1981).

We plotted tissue loads versus lumbar rotations to answer our second question: Is there a relationship between an individual's lumbar spine kinematics and the resulting tissue loads (Fig. 8)? While general trends existed such as higher disc loads at the beginning of sit-to-stand and higher facet forces at the end of sit-to-stand, no clear relationships between variables arose for either participant group. This result is likely due to differences in whole-body coordination (Fig. 6) and different muscle forces among individuals (Fig. 7) leading to a variety of distributions in tissue-level load transfer. These results underscore the importance of participant specificity and the potential benefits of individualized rehabilitation strategies that take both kinetics and kinematics into account.

Incorporation of the FE model in the multiscale modeling workflow enabled estimates of *in vivo* field variables such as annulus fibrosis stress across different participants and trials. Fig. 9 illustrates an example of the vM stress field in the posterior region of the L4–L5 annulus fibrosis for a single participant with TTA. High stress was observed at lift-off with the moment of peak stress occurring shortly after and coinciding with the moment of peak lateral bending. For all participants, peak annulus vM stress occurred at the inner posterior region of the annulus, similar to previous findings that show the initiation and propagation of annulus fibrosis damage to occur in the inner posterior region of the disc (Shahraki et al. 2015). The location of peak stress corresponded to the dominant and intact sides of the inner postero-lateral region for able-bodied participants and participants with TTA, respectively. The annulus stress continued to decrease and move toward the mid-sagittal plane as participants progressed to a less flexed posture throughout sit-to-stand (Fig. 9).

The location of peak annulus vM stress predicted by the multiscale model, in the postero-lateral region of the disc, was consistent with previous reports (Shahraki et al. 2015;

Bogduk 2012; McNally et al. 1996), and validation tests demonstrated the credibility of our intervertebral disc model (Figs. 2–4). Thus, we feel confident in the overall validity of our findings. But the magnitude of annulus stress predicted in this study (0.85–11.6 MPa during sit-to-stand) appears high. Experimental studies have shown that although the annulus itself is able to sustain high stress in compression (>30 MPa), the endplates fail much sooner (<5 MPa) (Bogduk 2012). In the computational modeling literature, many FE models of the intervertebral disc have been described (Dreischarf et al. 2014; Ayturk and Puttlitz 2011; Kiapour et al. 2012; Little et al. 2008; Liu et al. 2011; Park et al. 2013; Schmidt et al. 2012; Shirazi-Adl 1994; Zander et al. 2009; Campbell et al. 2016), but vM stress in the annulus has been rarely reported. There are no published data we are aware of for annulus vM stress under realistic *in vivo* loading conditions. Goto et al. found a peak vM stress of 0.87 MPa in the posterior portion of the L4–L5 disc and 18.40 MPa in the vertebral endplate when a 15 Nm pure flexion moment was applied Goto et al. (2002), but their mesh was very coarse, which can lead to inaccurate results from an FE model. Rohlmann et al. found peak vM stress < 6 MPa for applied pure moments of 10 Nm (Rohlmann et al. 2006). For computational efficiency, our FE model simulated the bones and endplates as rigid. This simplification produced local stress peaks immediately adjacent to the endplates due to the discontinuity in stiffness at the disc/bone boundary. For this reason, stress results from annulus elements adjacent to the endplates were discarded from our results, but the local peaks likely caused some elevation of stress values throughout the annulus. While several previous studies have also modeled bones and endplates as rigid (Cegoñino et al. 2014; Coombs et al. 2013; Dreischarf et al. 2014; Little et al. 2007; Moramarco et al. 2010; Rao 2012), it will be important to incorporate a more accurate tissue stiffness gradient at the disc/bone boundary for future models that aim to make accurate predictions of intervertebral disc stresses.

Normalized L4–L5 IDP predicted by our model (Fig. 10) agreed well with a previous report of normalized *in vivo* disc pressure during sit-to-stand (Wilke et al. 2001) as we expected. The multiscale model estimates for absolute L4–L5 IDP among able-bodied participants during upright standing (or the end of sit-to-stand) were similar to the *in vivo* data. However, all model estimates for participants with TTA predicted higher IDP than the reported *in vivo* value (Fig. 10). This difference is not surprising and can be attributed to the greater abdominal force (Fig. 7) and greater lumbar flexion angle (Fig. 6) observed in participants with TTA. In addition, the participant in Wilke et al. (2001) did not have an amputation. Currently, no *in vivo* values of IDP have been reported for people with a lower-limb amputation.

To provide a more direct IDP comparison, an able-bodied participant in the present study (AB1) was identified (post

hoc) with anthropometry (height = 175 cm, weight = 70 kg) that matched very closely to the participant in Wilke et al. (2001) (height = 174 cm, weight = 72 kg). Multiscale estimates for AB1's disc pressure during upright standing were nearly identical to the in vivo value (Fig. 11). However, both the musculoskeletal and FE models overestimated peak IDP during sit-to-stand for AB1 relative to the value reported in Wilke et al. (2001). This discrepancy could be caused by realistic differences in motion and loading. The exact trunk-pelvis kinematics for the participant in Wilke et al. (2001) during sit-to-stand were not reported and are likely different than the AB1 participant in this study. The average initial flexion angle for AB1 across the five sit-to-stand trials was 10°. As demonstrated in Fig. 8, a flexion angle of 10° was associated with a range of possible IDP values in the present study, an effect driven by variations in trunk kinematics and muscle force distribution (Figs. 6, 7). It is challenging to compare biomechanical model estimates to in vivo values for dynamic activities of daily living when in vivo values are reported for only a single participant and trial. In light of these considerations, we would argue that the multiscale estimates of disc pressure are reasonable.

This study had several limitations. Although our multiscale framework comprised previously validated models at the whole-body (Actis et al. 2018a, b) and tissue-level (Campbell et al. 2016) length scales, additional validation of the combined multiscale model must be conducted to increase confidence in its suitability for clinical application. Indeed, validation of such a model is a highly targeted activity (i.e., focusing on specific outputs for specific contexts of use), and it is much more of a process than a discrete task. Successful completion of musculoskeletal simulations for some participants required increases in the default muscle strength. Incorporating participant-specific lumbar spine geometry, muscle physiology, muscle attachment locations, ligament properties, and kinematic rhythms may improve the muscle force and joint loading estimates from the musculoskeletal model (Arshad et al. 2016; Bruno et al. 2017; Bayoglu et al. 2019), which may also affect tissue loading estimates from the FE model (Dehghan-Hamani et al. 2019; Zanjani-Pour et al. 2016). Incorporation of greater subject-specificity in both models may reduce the need for increases in muscle strength, which may influence tissue-level load transfer. Able-bodied participants in this study were mostly younger, smaller females, whereas the participants with TTA were older, larger males. To mitigate differences in height and weight, loading outcomes were normalized by body weight. It is a challenge to recruit well-matched participants for biomechanics studies, especially when targeting persons with amputation, but we acknowledge that better controlling for age, height, weight, and gender may provide better comparisons between groups in future studies. In order to gain better understanding of tissue-level load transfer for

relevant populations during a variety of activities of daily living, many different tasks (e.g., lifting, squatting, walking) should be investigated. Lastly, including pain as a factor will be critical for future work to determine potential tissue-level differences between people with and without LBP. These future investigations will shed light on participant-specific tissue-level load transfer during a variety of daily activities and aid in targeted clinical care for individuals with pain originating from biomechanical factors.

Acknowledgements This work is supported in part by the National Science Foundation Graduate Research Fellowship No. DGE-1646713.

References

- Actis JA, Honegger JD, Gates DH, Petrella AJ, Nolasco LA, Silverman AK (2018a) Validation of lumbar spine loading from a musculoskeletal model including the lower limbs and lumbar spine. *J Biomech* 68:107–114. <https://doi.org/10.1016/j.jbiomech.2017.12.001>
- Actis JA, Nolasco LA, Gates DH, Silverman AK (2018b) Lumbar loads and trunk kinematics in people with a transtibial amputation during sit-to-stand. *J Biomech* 69:1–9. <https://doi.org/10.1016/j.jbiomech.2017.12.030>
- Adams MA, Green TP, Dolan P (1994) The strength in anterior bending of lumbar intervertebral discs. *Spine* 19(19):2197–2203
- Adams MA, Freeman BJ, Morrison HP, Nelson IW, Dolan P (2000) Mechanical initiation of intervertebral disc degeneration. *Spine* 25(13):1625–1636
- Affolter C, Kedzierska J, Vielma T, Weisse B, Aiyangar A (2020) Estimating lumbar passive stiffness behaviour from subject-specific finite element models and in vivo 6dof kinematics. *J Biomech*. <https://doi.org/10.1016/j.jbiomech.2020.109681>
- Andersson G, Ortengren R, Nachemson A (1977) Intradiscal pressure, intra-abdominal pressure and myoelectric back muscle activity related to posture and loading. *Clin Orthop Relat R* 129:156–164
- van Arkel RJ, Modenese L, Phillips AT, Jeffers JR (2013) Hip abduction can prevent posterior edge loading of hip replacements. *J Orthop Res* 31(8):1172–1179. <https://doi.org/10.1002/jor.22364>
- Arshad R, Zander T, Dreischarf M, Schmidt H (2016) Influence of lumbar spine rhythms and intra-abdominal pressure on spinal loads and trunk muscle forces during upper body inclination. *Med Eng Phys* 38(4):333–338. <https://doi.org/10.1016/j.medengphys.2016.01.013>
- Asano S, Kaneda K, Umehara S, Tadano S (1992) The mechanical properties of the human l4–5 functional spinal unit during cyclic loading: the structural effects of the posterior elements. *Spine* 17(11):1343–1352. <https://doi.org/10.1097/00007632-19921000-00014>
- Ayturk UM, Puttlitz CM (2011) Parametric convergence sensitivity and validation of a finite element model of the human lumbar spine. *Comput Method Biomech* 14(8):695–705. <https://doi.org/10.1080/10255842.2010.493517>
- Azari F, Arjmand N, Shirazi-Adl A, Rahimi-Moghaddam T (2018) A combined passive and active musculoskeletal model study to estimate l4–l5 load sharing. *J Biomech* 70:157–165. <https://doi.org/10.1016/j.jbiomech.2017.04.026>
- Bassani T, Stucovitz E, Qian Z, Briguglio M, Galbusera F (2017) Validation of the anybody full body musculoskeletal model in computing lumbar spine loads at l4/l5 level. *J Biomech* 58:89–96. <https://doi.org/10.1016/j.jbiomech.2017.04.025>

- Bayoglu R, Geeraedts L, Groenen KH, Verdonshot N, Koopman B, Homminga J (2017) Twente spine model: a complete and coherent dataset for musculo-skeletal modeling of the lumbar region of the human spine. *J Biomech* 53:111–119. <https://doi.org/10.1016/j.jbiomech.2017.01.009>
- Bayoglu R, Guldeniz O, Verdonshot N, Koopman B, Homminga J (2019) Sensitivity of muscle and intervertebral disc force computations to variations in muscle attachment sites. *Comput Methods Biomech Biomed Eng* 22(14):1135–1143. <https://doi.org/10.1080/10255842.2019.1644502>
- Beaucage-Gauvreau E, Robertson WS, Brandon SC, Fraser R, Freeman BJ, Graham RB, Thewlis D, Jones CF (2019) Validation of an opensim full-body model with detailed lumbar spine for estimating lower lumbar spine loads during symmetric and asymmetric lifting tasks. *Comput Method Biomech* 22(5):451–464. <https://doi.org/10.1080/10255842.2018.1564819>
- Bergström P (2006) Iterative closest point method. <https://www.mathworks.com/matlabcentral/fileexchange/12627-iterative-closest-point-method>
- Bogduk N (2012) *Clinical and radiological anatomy of the lumbar spine*. Elsevier Health Sciences, Amsterdam
- Brenner DJ, Hall EJ (2007) Computed tomography an increasing source of radiation exposure. *New Engl J Med* 357(22):2277–2284
- Brinckmann P, Grootenboer H (1991) Change of disc height, radial disc bulge, and intradiscal pressure from discectomy. An in vitro investigation on human lumbar discs. *Spine* 16(6):641–646. <https://doi.org/10.1097/00007632-199106000-00008>
- Brown T, Hansen RJ, Yorra AJ (1957) Some mechanical tests on the lumbosacral spine with particular reference to the intervertebral discs: a preliminary report. *J Bone Joint Surg* 39(5):1135–1164
- Bruno AG, Bouxsein ML, Anderson DE (2015) Development and validation of a musculoskeletal model of the fully articulated thoracolumbar spine and rib cage. *J Biomech Eng* 137(8):081003. <https://doi.org/10.1115/1.4030408>
- Bruno AG, Mokhtarzadeh H, Allaire BT, Velie KR, De Paolis Kaluza MC, Anderson DE, Bouxsein ML (2017) Incorporation of ct-based measurements of trunk anatomy into subject-specific musculoskeletal models of the spine influences vertebral loading predictions. *J Orthop Res* 35(10):2164–2173. <https://doi.org/10.1002/jor.23524>
- Burger H, Kuželički J, Marinček Č (2005) Transition from sitting to standing after trans-femoral amputation. *Prosthet Orthot Int* 29(2):139–151. <https://doi.org/10.1080/03093640500199612>
- Burke M, Roman V, Wright V (1978) Bone and joint changes in lower limb amputees. *Ann Rheum Dis* 37(3):252–254
- Burnett DR, Campbell-Kyureghyan NH, Cerrito PB, Quesada PM (2011) Symmetry of ground reaction forces and muscle activity in asymptomatic subjects during walking, sit-to-stand, and stand-to-sit tasks. *J Electromyogr Kines* 21(4):610–615. <https://doi.org/10.1016/j.jelekin.2011.03.006>
- Bussmann JB, Grootcholten EA, Stam HJ (2004) Daily physical activity and heart rate response in people with a unilateral transtibial amputation for vascular disease. *Arch Phys Med Rehab* 85(2):240–244. [https://doi.org/10.1016/S0003-9993\(03\)00485-4](https://doi.org/10.1016/S0003-9993(03)00485-4)
- Bussmann JB, Schrauwen HJ, Stam HJ (2008) Daily physical activity and heart rate response in people with a unilateral traumatic transtibial amputation. *Arch Phys Med Rehab* 89(3):430–434. <https://doi.org/10.1016/j.apmr.2007.11.012>
- Callaghan JP, McGill SM (2001) Intervertebral disc herniation: studies on a porcine model exposed to highly repetitive flexion/extension motion with compressive force. *Clin Biomech* 16(1):28–37. [https://doi.org/10.1016/S0268-0033\(00\)00063-2](https://doi.org/10.1016/S0268-0033(00)00063-2)
- Campbell J, Coombs D, Rao M, Rullkoetter P, Petrella A (2016) Automated finite element meshing of the lumbar spine: verification and validation with 18 specimen-specific models. *J Biomech* 49(13):2669–2676. <https://doi.org/10.1016/j.jbiomech.2016.05.025>
- Campbell JQ, Petrella AJ (2015) An automated method for landmark identification and finite-element modeling of the lumbar spine. *IEEE Trans Biomed Eng* 62(11):2709–2716. <https://doi.org/10.1109/TBME.2015.2444811>
- Cegoñino J, Moramarco V, Calvo-Echenique A, Pappalettere C, Pérez Del Palomar A (2014) A constitutive model for the annulus of human intervertebral disc: implications for developing a degeneration model and its influence on lumbar spine functioning. *J Appl Math*. <https://doi.org/10.1155/2014/658719>
- Cholewicki J, McGill SM (1996) Mechanical stability of the in vivo lumbar spine: implications for injury and chronic low back pain. *Clin Biomech* 11(1):1–15. [https://doi.org/10.1016/0268-0033\(95\)00035-6](https://doi.org/10.1016/0268-0033(95)00035-6)
- Cholewicki J, McGill SM, Norman RW (1995) Comparison of muscle forces and joint load from an optimization and emg assisted lumbar spine model: towards development of a hybrid approach. *J Biomech* 28(3):321–331. [https://doi.org/10.1016/0021-9290\(94\)00065-C](https://doi.org/10.1016/0021-9290(94)00065-C)
- Christophy M, Senan NAF, Lotz JC, O'Reilly OM (2012) A musculo-skeletal model for the lumbar spine. *Biomech Model Mechan* 11(1–2):19–34. <https://doi.org/10.1007/s10237-011-0290-6>
- Cohen J (1992) A power primer. *Psychol Bull* 112(1):155
- Coombs D, Bushelow M, Laz P, Rao M, Rullkoetter P (2013) Stepwise validated finite element model of the human lumbar spine. In: *front biomed devices*. American Society of Mechanical Engineers, vol 56000, p V001T01A004
- De Zee M, Hansen L, Wong C, Rasmussen J, Simonsen EB (2007) A generic detailed rigid-body lumbar spine model. *J Biomech* 40(6):1219–1227. <https://doi.org/10.1016/j.jbiomech.2006.05.030>
- Dehghan-Hamani I, Arjmand N, Shirazi-Adl A (2019) Subject-specific loads on the lumbar spine in detailed finite element models scaled geometrically and kinematic-driven by radiography images. *Int J Numer Meth Biol* 35(4):e3182. <https://doi.org/10.1002/cnm.3182>
- Devan H, Hendrick P, Ribeiro DC, Hale LA, Carman A (2014) Asymmetrical movements of the lumbopelvic region: is this a potential mechanism for low back pain in people with lower limb amputation? *Med Hypotheses* 82(1):77–85. <https://doi.org/10.1016/j.mehy.2013.11.012>
- Dreischarf M, Rohlmann A, Zhu R, Schmidt H, Zander T (2013) Is it possible to estimate the compressive force in the lumbar spine from intradiscal pressure measurements? a finite element evaluation. *Med Eng Phys* 35(9):1385–1390. <https://doi.org/10.1016/j.medengphy.2013.03.007>
- Dreischarf M, Zander T, Shirazi-Adl A, Puttlitz C, Adam C, Chen C, Goel V, Kiapour A, Kim Y, Labus K et al. (2014) Comparison of eight published static finite element models of the intact lumbar spine: predictive power of models improves when combined together. *J Biomech* 47(8):1757–1766. <https://doi.org/10.1016/j.jbiomech.2014.04.002>
- Dreischarf M, Shirazi-Adl A, Arjmand N, Rohlmann A, Schmidt H (2016) Estimation of loads on human lumbar spine: a review of in vivo and computational model studies. *J Biomech* 49(6):833–845. <https://doi.org/10.1016/j.jbiomech.2015.12.038>
- Eberlein R, Holzapfel GA, Schulze-Bauer CA (2001) An anisotropic model for annulus tissue and enhanced finite element analyses of intact lumbar disc bodies. *Comput Method Biomech* 4(3):209–229
- Eberlein R, Holzapfel GA, Fröhlich M (2004) Multi-segment fea of the human lumbar spine including the heterogeneity of the annulus fibrosus. *Comput Mech* 34(2):147–163. <https://doi.org/10.1007/s00466-004-0563-3>
- Emanuel KS, van der Veen AJ, Rustenburg CM, Smit TH, Kingma I (2018) Osmosis and viscoelasticity both contribute to

- time-dependent behaviour of the intervertebral disc under compressive load: A caprine in vitro study. *J Biomech* 70:10–15. <https://doi.org/10.1016/j.jbiomech.2017.10.010>
- Fairbank JC, Pynsent PB (2000) The Oswestry disability index. *Spine* 25(22):2940–2953
- Fujii R, Sakaura H, Mukai Y, Hosono N, Ishii T, Iwasaki M, Yoshikawa H, Sugamoto K (2007) Kinematics of the lumbar spine in trunk rotation: in vivo three-dimensional analysis using magnetic resonance imaging. *Eur Spine J* 16(11):1867–1874. <https://doi.org/10.1007/s00586-007-0373-3>
- Gardner-Morse MG, Stokes IA (1998) The effects of abdominal muscle coactivation on lumbar spine stability. *Spine* 23(1):86–91
- Gasser TC, Ogdén RW, Holzapfel GA (2005) Hyperelastic modelling of arterial layers with distributed collagen fibre orientations. *J R Soc Interface* 3(6):15–35. <https://doi.org/10.1098/rsif.2005.0073>
- Ghezelbash F, Shirazi-Adl A, Arjmand N, El-Ouaaid Z, Plamondon A (2016) Subject-specific biomechanics of trunk: musculoskeletal scaling, internal loads and intradiscal pressure estimation. *Bio-mech Model Mechan* 15(6):1699–1712. <https://doi.org/10.1007/s10237-016-0792-3>
- Ghezelbash F, Schmidt H, Shirazi-Adl A, El-Rich M (2019a) Internal load-sharing in the human passive lumbar spine: review of in vitro and finite element model studies. *J Biomech*. <https://doi.org/10.1016/j.jbiomech.2019.109441>
- Ghezelbash F, Shirazi-Adl A, Baghani M, Eskandari AH (2019b) On the modeling of human intervertebral disc annulus fibrosus: elastic, permanent deformation and failure responses. *J Biomech*. <https://doi.org/10.1016/j.jbiomech.2019.109463>
- Goto K, Tajima N, Chosa E, Totoribe K, Kuroki H, Arizumi Y, Arai T (2002) Mechanical analysis of the lumbar vertebrae in a three-dimensional finite element method model in which intradiscal pressure in the nucleus pulposus was used to establish the model. *J Orthop Sci* 7(2):243–246
- Han KS, Zander T, Taylor WR, Rohlmann A (2012) An enhanced and validated generic thoraco-lumbar spine model for prediction of muscle forces. *Med Eng Phys* 34(6):709–716. <https://doi.org/10.1016/j.medengphy.2011.09.014>
- Hendershot BD, Wolf EJ (2014) Three-dimensional joint reaction forces and moments at the low back during over-ground walking in persons with unilateral lower-extremity amputation. *Clin Biomech* 29(3):235–242. <https://doi.org/10.1016/j.clinbiomech.2013.12.005>
- Hendershot BD, Wolf EJ (2015) Persons with unilateral transfemoral amputation have altered lumbosacral kinetics during sitting and standing movements. *Gait Posture* 42(2):204–209. <https://doi.org/10.1016/j.gaitpost.2015.05.011>
- Herzog W (1987) Individual muscle force estimations using a nonlinear optimal design. *J Neurosci Meth* 21(2–4):167–179. [https://doi.org/10.1016/0165-0270\(87\)90114-2](https://doi.org/10.1016/0165-0270(87)90114-2)
- Highsmith MJ, Goff LM, Lewandowski AL, Farrokhi S, Hendershot BD, Hill OT, Rabago CA, Russell-Espinoza E, Orriola JJ, Mayer JM (2019) Low back pain in persons with lower extremity amputation: a systematic review of the literature. *Spine J* 19(3):552–563. <https://doi.org/10.1016/j.spinee.2018.08.011>
- Hill AV (1938) The heat of shortening and the dynamic constants of muscle. *P R Soc Lond B Biol* 126(843):136–195
- Holzapfel GA, Gasser TC, Ogdén RW (2000) A new constitutive framework for arterial wall mechanics and a comparative study of material models. *J Elasticity* 61(1–3):1–48
- Holzapfel GA, Schulze-Bauer C, Feigl G, Regitnig P (2005) Single lamellar mechanics of the human lumbar annulus fibrosus. *Bio-mech Model Mechan* 3(3):125–140. <https://doi.org/10.1007/s10237-004-0053-8>
- Honegger JD, Hall BM, Knutson K, Lo AY, Nobarani H, Pathare NB, Ziegler NC, Petrella AJ (2019) Sensitivity of lumbar spine mechanics to variations in intervertebral disc hyperelastic material parameters using a finite element model of a functional spinal unit. In: Proceedings of the 2019 Annual Meeting for the Orthopaedic Research Society, vol 44. <https://www.ors.org/Transactions/65/0860.pdf>
- Ignasiak D, Dendorfer S, Ferguson SJ (2016) Thoracolumbar spine model with articulated ribcage for the prediction of dynamic spinal loading. *J Biomech* 49(6):959–966. <https://doi.org/10.1016/j.jbiomech.2015.10.010>
- Jamison D, Cannella M, Pierce EC, Marcolongo MS (2013) A comparison of the human lumbar intervertebral disc mechanical response to normal and impact loading conditions. *J Biomech Eng*. <https://doi.org/10.1115/1.4024828>
- Khoddam-Khorasani P, Arjmand N, Shirazi-Adl A (2018) Trunk hybrid passive-active musculoskeletal modeling to determine the detailed t12–s1 response under in vivo loads. *Ann Biomed Eng* 46(11):1830–1843. <https://doi.org/10.1007/s10439-018-2078-7>
- Kiapour A, Ambati D, Hoy RW, Goel VK (2012) Effect of graded facetectomy on biomechanics of dynesys dynamic stabilization system. *Spine* 37(10):E581–E589. <https://doi.org/10.1097/BRS.0b013e3182463775>
- Lalonde NM, Petit Y, Aubin CE, Wagnac E, Arnoux PJ (2013) Method to geometrically personalize a detailed finite-element model of the spine. *IEEE Trans Biomed Eng* 60(7):2014–2021. <https://doi.org/10.1109/TBME.2013.2246865>
- Lavecchia C, Espino D, Moerman K, Tse K, Robinson D, Lee P, Shepherd D (2018) Lumbar model generator: a tool for the automated generation of a parametric scalable model of the lumbar spine. *J R Soc Interface* 15(138):20170829. <https://doi.org/10.1098/rsif.2017.0829>
- Little JP, Adam CJ, Evans JH, Pettet GJ, Pearcy MJ (2007) Nonlinear finite element analysis of annular lesions in the L4/5 intervertebral disc. *J Biomech* 40(12):2744–2751. <https://doi.org/10.1016/j.jbiomech.2007.01.007>
- Little JP, De Visser H, Pearcy MJ, Adam CJ (2008) Are coupled rotations in the lumbar spine largely due to the osseo-ligamentous anatomy? a modeling study. *Comput Method Biomech* 11(1):95–103. <https://doi.org/10.1080/10255840701552143>
- Liu CL, Zhong ZC, Hsu HW, Shih SL, Wang ST, Hung C, Chen CS (2011) Effect of the cord pretension of the dynesys dynamic stabilization system on the biomechanics of the lumbar spine: a finite element analysis. *Eur Spine J* 20(11):1850–1858. <https://doi.org/10.1007/s00586-011-1817-3>
- Liu T, Khalaf K, Naserkhaki S, El-Rich M (2018) Load-sharing in the lumbosacral spine in neutral standing & flexed postures—a combined finite element and inverse static study. *J Biomech* 70:43–50. <https://doi.org/10.1016/j.jbiomech.2017.10.033>
- Lu TW, O'Connor J (1999) Bone position estimation from skin marker co-ordinates using global optimisation with joint constraints. *J Biomech* 32(2):129–134. [https://doi.org/10.1016/S0021-9290\(98\)00158-4](https://doi.org/10.1016/S0021-9290(98)00158-4)
- Malandrino A, Noailly J, Lacroix D (2013) Regional annulus fibre orientations used as a tool for the calibration of lumbar intervertebral disc finite element models. *Comput Methods Biomech Biomed Eng* 16(9):923–928. <https://doi.org/10.1080/10255842.2011.644539>
- Marini G, Studer H, Huber G, Püschel K, Ferguson SJ (2016) Geometrical aspects of patient-specific modelling of the intervertebral disc: Collagen fibre orientation and residual stress distribution. *Bio-mech Model Mechan* 15(3):543–560. <https://doi.org/10.1007/s10237-015-0709-6>
- Markolf KL, Morris JM (1974) The structural components of the intervertebral disc: a study of their contributions to the ability of the disc to withstand compressive forces. *J Bone Joint Surg* 56(4):675–687
- Marras WS, Lavender SA, Leurgans SE, Rajulu SL, Allread SWG, Fathallah FA, Ferguson SA (1993) The role of dynamic

- three-dimensional trunk motion in occupationally-related. *Spine* 18(5):617–628
- McNally DS, Shackelford IM, Goodship AE, Mulholland RC (1996) In vivo stress measurement can predict pain on discography. *Spine* 21(22):2580–2587
- Moramarcò Vd, Del Palomar AP, Pappalettere C, Doblaré M (2010) An accurate validation of a computational model of a human lumbosacral segment. *J Biomech* 43(2):334–342. <https://doi.org/10.1016/j.jbiomech.2009.07.042>
- Morgenroth DC, Orendurff MS, Shakir A, Segal A, Shofer J, Czerniecki JM (2010) The relationship between lumbar spine kinematics during gait and low-back pain in transfemoral amputees. *Am J Phys Med Rehabil* 89(8):635–643. <https://doi.org/10.1097/PHM.0b013e3181e71d90>
- Nachemson A (1960) Lumbar intradiscal pressure: experimental studies on post-mortem material. *Acta Orthop Scand* 31(sup43):1–104
- Nachemson A (1965) The effect of forward leaning on lumbar intradiscal pressure. *Acta Orthop Scand* 35(1–4):314–328
- Nachemson A, Elfström G (1970) Intravital dynamic pressure measurements in lumbar discs. *Scand J Rehabil Med* 2(suppl 1):1–40
- Nachemson A, Morris JM (1964) In vivo measurements of intradiscal pressure: discometry, a method for the determination of pressure in the lower lumbar discs. *J Bone Joint Surg* 46(5):1077–1092
- Nikkhoo M, Wang JL, Parnianpour M, El-Rich M, Khalaf K (2018) Biomechanical response of intact, degenerated and repaired intervertebral discs under impact loading-ex-vivo and in-silico investigation. *J Biomech* 70:26–32. <https://doi.org/10.1016/j.jbiomech.2018.01.026>
- Örtengren R, Andersson GB, Nachemson AL (1981) Studies of relationships between lumbar disc pressure, myoelectric back muscle activity, and intra-abdominal (intra-gastric) pressure. *Spine* 6(1):98–103
- Park WM, Kim K, Kim YH (2013) Effects of degenerated intervertebral discs on intersegmental rotations, intradiscal pressures, and facet joint forces of the whole lumbar spine. *Comput Biol Med* 43(9):1234–1240. <https://doi.org/10.1016/j.compbiomed.2013.06.011>
- Pearcy MJ (1985) Stereo radiography of lumbar spine motion. *Acta Orthop Scand* 56(sup212):1–45
- Phillips AT, Villette CC, Modenese L (2015) Femoral bone mesoscale structural architecture prediction using musculoskeletal and finite element modelling. *Int Biomech* 2(1):43–61. <https://doi.org/10.1080/23335432.2015.1017609>
- Raabe ME, Chaudhari AM (2016) An investigation of jogging biomechanics using the full-body lumbar spine model: Model development and validation. *J Biomech* 49(7):1238–1243. <https://doi.org/10.1016/j.jbiomech.2016.02.046>
- Rao M (2012) Explicit finite element modeling of the human lumbar spine. University of Denver. <https://digitalcommons.du.edu/etd/906>
- Rohlmann A, Bergmann G, Graichen F (1999) Loads on internal spinal fixators measured in different body positions. *Eur Spine J* 8(5):354–359
- Rohlmann A, Neller S, Claes L, Bergmann G, Wilke HJ (2001) Influence of a follower load on intradiscal pressure and intersegmental rotation of the lumbar spine. *Spine* 26(24):E557–E561
- Rohlmann A, Zander T, Schmidt H, Wilke HJ, Bergmann G (2006) Analysis of the influence of disc degeneration on the mechanical behaviour of a lumbar motion segment using the finite element method. *J Biomech* 39(13):2484–2490. <https://doi.org/10.1016/j.jbiomech.2005.07.026>
- Rohlmann A, Zander T, Rao M, Bergmann G (2009) Applying a follower load delivers realistic results for simulating standing. *J Biomech* 42(10):1520–1526. <https://doi.org/10.1016/j.jbiomech.2009.03.048>
- Rohlmann A, Dreischarf M, Zander T, Graichen F, Strube P, Schmidt H, Bergmann G (2013) Monitoring the load on a telemeterised vertebral body replacement for a period of up to 65 months. *Eur Spine J* 22(11):2575–2581. <https://doi.org/10.1007/s00586-013-3057-1>
- Rozumalski A, Schwartz MH, Wervev R, Swanson A, Dykes DC, Novacheck T (2008) The in vivo three-dimensional motion of the human lumbar spine during gait. *Gait Posture* 28(3):378–384. <https://doi.org/10.1016/j.gaitpost.2008.05.005>
- Rueda FM, Diego IMA, Sánchez AM, Tejada MC, Montero FMR, Page JCM (2013) Knee and hip internal moments and upper-body kinematics in the frontal plane in unilateral transtibial amputees. *Gait Posture* 37(3):436–439. <https://doi.org/10.1016/j.gaitpost.2012.08.019>
- Sato K, Kikuchi S, Yonezawa T (1999) In vivo intradiscal pressure measurement in healthy individuals and in patients with ongoing back problems. *Spine* 24(23):2468
- Schmidt H, Shirazi-Adl A, Galbusera F, Wilke HJ (2010) Response analysis of the lumbar spine during regular daily activities—a finite element analysis. *J Biomech* 43(10):1849–1856. <https://doi.org/10.1016/j.jbiomech.2010.03.035>
- Schmidt H, Galbusera F, Rohlmann A, Zander T, Wilke HJ (2012) Effect of multilevel lumbar disc arthroplasty on spine kinematics and facet joint loads in flexion and extension: a finite element analysis. *Eur Spine J* 21(5):663–674. <https://doi.org/10.1007/s00586-010-1382-1>
- Senteler M, Weisse B, Rothenfluh DA, Snedeker JG (2016) Intervertebral reaction force prediction using an enhanced assembly of opensim models. *Comput Methods Biomech Biomed Eng* 19(5):538–548. <https://doi.org/10.1080/10255842.2015.1043906>
- Shahraki N, Fatemi A, Agarwal A et al. (2015) Failure criteria for prediction of clinically relevant damage of annulus fibrosus. *Spine Res*. <https://doi.org/10.21767/2471-8173.100007>
- Shirazi-Adl A (1994) Biomechanics of the lumbar spine in sagittal/lateral moments. *Spine* 19(21):2407–2414. <https://doi.org/10.1097/00007632-199410000-00007>
- Shojaei I, Hendershot BD, Wolf EJ, Bazrgari B (2016) Persons with unilateral transfemoral amputation experience larger spinal loads during level-ground walking compared to able-bodied individuals. *Clin Biomech* 32:157–163. <https://doi.org/10.1016/j.clinbiomech.2015.11.018>
- Shojaei I, Hendershot BD, Acasio JC, Dearth CL, Ballard M, Bazrgari B (2019) Trunk muscle forces and spinal loads in persons with unilateral transfemoral amputation during sit-to-stand and stand-to-sit activities. *Clin Biomech* 63:95–103. <https://doi.org/10.1016/j.clinbiomech.2019.02.021>
- Silverman AK, Neptune RR (2012) Muscle and prosthesis contributions to amputee walking mechanics: a modeling study. *J Biomech* 45(13):2271–2278. <https://doi.org/10.1016/j.jbiomech.2012.06.008>
- Šljajpah S, Kamnik R, Burger H, Bajd T, Munih M (2013) Asymmetry in sit-to-stand movement in patients following transtibial amputation and healthy individuals. *Int J Rehabil Res* 36(3):275–283. <https://doi.org/10.1097/MRR.0b013e318283606235>
- Smith DG, Ehde DM, Legro MW, Reiber GE, del Aguila M, Boone DA (1999) Phantom limb, residual limb, and back pain after lower extremity amputations. *Clin Orthop Relat R* 361:29–38
- Stokes IA, Henry SM, Single RM (2003) Surface emg electrodes do not accurately record from lumbar multifidus muscles. *Clin Biomech* 18(1):9–13. [https://doi.org/10.1016/S0268-0033\(02\)00140-7](https://doi.org/10.1016/S0268-0033(02)00140-7)
- Swärd L, Hellström M, Jacobsson B, Nyman R, Peterson L (1991) Disc degeneration and associated abnormalities of the spine in elite gymnasts. A magnetic resonance imaging study. *Spine* 16(4):437–443. <https://doi.org/10.1097/00007632-199104000-00009>

- Takahashi I, Si Kikuchi, Sato K, Sato N (2006) Mechanical load of the lumbar spine during forward bending motion of the trunk—a biomechanical study. *Spine* 31(1):18–23. <https://doi.org/10.1097/01.brs.0000192636.69129.fb>
- Tencer A, Ahmed A, Burke D (1982) Some static mechanical properties of the lumbar intervertebral joint, intact and injured. *J Biomech Eng* 104(3):193–201. <https://doi.org/10.1115/1.3138348>
- Thelen DG (2003) Adjustment of muscle mechanics model parameters to simulate dynamic contractions in older adults. *J Biomech Eng* 125(1):70–77. <https://doi.org/10.1115/1.1531112>
- Toumanidou T, Noailly J (2015) Musculoskeletal modeling of the lumbar spine to explore functional interactions between back muscle loads and intervertebral disk multiphysics. *Front Bioeng Biotech* 3:111. <https://doi.org/10.3389/fbioe.2015.00111>
- Van Dieën J, Kingma I (2005) Effects of antagonistic co-contraction on differences between electromyography based and optimization based estimates of spinal forces. *Ergonomics* 48(4):411–426. <https://doi.org/10.1080/00140130512331332918>
- Verdun FR, Bochud F, Gundinchet F, Aroua A, Schnyder P, Meuli R (2008) Quality initiatives radiation risk: what you should know to tell your patient. *Radiographics* 28(7):1807–1816. <https://doi.org/10.1148/rg.287085042>
- Vos T, Allen C, Arora M, Barber RM, Bhutta ZA, Brown A, Carter A, Casey DC, Charlson FJ, Chen AZ et al. (2016) Global, regional, and national incidence, prevalence, and years lived with disability for 310 diseases and injuries, 1990–2015: a systematic analysis for the global burden of disease study 2015. *Lancet* 388(10053):1545–1602. [https://doi.org/10.1016/S0140-6736\(16\)31678-6](https://doi.org/10.1016/S0140-6736(16)31678-6)
- Wächter A, Biegler LT (2006) On the implementation of an interior-point filter line-search algorithm for large-scale nonlinear programming. *Math Program* 106(1):25–57. <https://doi.org/10.1007/s10107-004-0559-y>
- Wilber C, Holland G, Madison R, Loy S (1995) An epidemiological analysis of overuse injuries among recreational cyclists. *Int J Sports Med* 16(03):201–206. <https://doi.org/10.1055/s-2007-972992>
- Wilke HJ, Wenger K, Claes L (1998) Testing criteria for spinal implants: recommendations for the standardization of in vitro stability testing of spinal implants. *Eur Spine J* 7(2):148–154
- Wilke HJ, Neef P, Caimi M, Hoogland T, Claes LE (1999) New in vivo measurements of pressures in the intervertebral disc in daily life. *Spine* 24(8):755–762
- Wilke HJ, Neef P, Hinze B, Seidel H, Claes L (2001) Intradiscal pressure together with anthropometric data—a data set for the validation of models. *Clin Biomech* 16:S111–S126. [https://doi.org/10.1016/S0268-0033\(00\)00103-0](https://doi.org/10.1016/S0268-0033(00)00103-0)
- Wong KW, Luk KD, Leong JC, Wong SF, Wong KK (2006) Continuous dynamic spinal motion analysis. *Spine* 31(4):414–419. <https://doi.org/10.1097/01.brs.0000199955.87517.82>
- Xu M, Yang J, Lieberman IH, Haddas R (2017) Lumbar spine finite element model for healthy subjects: development and validation. *Comput Methods Biomech Biomed Eng* 20(1):1–15. <https://doi.org/10.1080/10255842.2016.1193596>
- Yoder AJ, Petrella AJ, Silverman AK (2015) Trunk-pelvis motion, joint loads, and muscle forces during walking with a transtibial amputation. *Gait Posture* 41(3):757–762. <https://doi.org/10.1016/j.gaitpost.2015.01.016>
- Zander T, Rohlmann A, Bergmann G (2009) Influence of different artificial disc kinematics on spine biomechanics. *Clin Biomech* 24(2):135–142. <https://doi.org/10.1016/j.clinbiomech.2008.11.008>
- Zanjani-Pour S, Winlove CP, Smith CW, Meakin JR (2016) Image driven subject-specific finite element models of spinal biomechanics. *J Biomech* 49(6):919–925. <https://doi.org/10.1016/j.jbiomech.2016.02.025>
- Zanjani-Pour S, Meakin JR, Breen A, Breen A (2018) Estimation of in vivo inter-vertebral loading during motion using fluoroscopic and magnetic resonance image informed finite element models. *J Biomech* 70:134–139. <https://doi.org/10.1016/j.jbiomech.2017.09.025>
- Zhu R, Zander T, Dreischarf M, Duda GN, Rohlmann A, Schmidt H (2013) Considerations when loading spinal finite element models with predicted muscle forces from inverse static analyses. *J Biomech* 46(7):1376–1378. <https://doi.org/10.1016/j.jbiomech.2013.03.003>